HELDA
HELSINGIN YLIOPISTO
HELSINGFORS UNIVERSITET
UNIVERSITY OF HELSINKI

UNIVERSITY OF HELSINKI

https://helda.helsinki.fi

SHANK3 conformation regulates direct actin binding and crosstalk with Rap1 signaling

Salomaa, Siiri

2021-11-22

Salomaa , S , Miihkinen , M , Kremneva , E , Paatero , I , Lilja , J , Jacquemet , G , Vuorio , J , Antenucci , L , Kogan , K , Nia , F H , Hollos , P , Isomursu , A , Vattulainen , I , Coffey , E T , Kreienkamp , H-J , Lappalainen , P & Ivaska , J 2021 , ' SHANK3 conformation regulates direct actin binding and crosstalk with Rap1 signaling ' , Current Biology , vol. 31 , no. 22 , pp. 4956-+ . https://doi.org/10.1016/j.cub.2021.09.022

http://hdl.handle.net/10138/350903
https://doi.org/10.1016/j.cub.2021.09.022

cc_by_nc_nd
acceptedVersion

Downloaded from Helda, University of Helsinki institutional repository.

This is an electronic reprint of the original article.

This reprint may differ from the original in pagination and typographic detail.

Please cite the original version.

SHANK3 conformation regulates direct actin binding and crosstalk with Rap1 signaling

Siiri I. Salomaa[1], Mitro Miihkinen[1], Elena Kremneva[2], Ilkka Paatero[1], Johanna Lilja[1], Guillaume Jacquemet[1,3], Joni Vuorio[4], Lina Antenucci[2], Konstantin Kogan[2], Fatemeh Hassani Nia[5], Patrik Hollos[1], Aleksi Isomursu[1], Ilpo Vattulainen[4], Eleanor T. Coffey[1], Hans-Jürgen Kreienkamp[5], Pekka Lappalainen[2] and Johanna Ivaska[1,6].

[1] Turku Bioscience Centre, University of Turku and Åbo Akademi University, Tykistökatu 6, Turku, FI-20520, Finland

[2] HiLIFE Institute of Biotechnology, University of Helsinki, Viikinkaari 5B, P.O. Box 56 FI-00014 Helsinki, Finland

[3] Faculty of Science and Engineering, Cell Biology, Åbo Akademi University, Tykistökatu 6, Turku, FI-20520, Finland

[4] Department of Physics, University of Helsinki, Gustaf Helströmin katu 2, Helsinki, Finland

[5] Institute for Human Genetics, University Medical Center Hamburg-Eppendorf, Martinistraße 52, 20251 Hamburg, Germany

[6] Department of Life Technologies, University of Turku, Tykistökatu 6, Turku, FI-20520, Finland

***Correspondence to lead contact:** Johanna Ivaska; johanna.ivaska@utu.fi

Running title: *SHANK3 regulates interplay between actin and integrins*

Summary

Actin-rich cellular protrusions direct versatile biological processes from cancer cell invasion to dendritic spine development. The stability, morphology and specific biological functions of these protrusions are regulated by crosstalk between three main signaling axes: integrins, actin regulators and small GTPases. SHANK3 is a multifunctional scaffold protein, interacting with several actin-binding proteins, and a well-established autism risk gene. Recently, SHANK3 was demonstrated to sequester integrin-activating small GTPases Rap1 and R-Ras to inhibit integrin activity via its N-terminal SPN-domain. Here, we demonstrate that in addition to scaffolding actin regulators and actin-binding proteins, SHANK3 interacts directly with actin through its SPN-domain. Molecular simulations and targeted mutagenesis of the SPN-ARR interface reveal that actin binding is inhibited by an intramolecular closed

conformation of SHANK3, where the adjacent ARR domain covers the actin-binding interface of the SPN-domain. Actin and Rap1 compete with each other for binding to SHANK3 and mutation of SHANK3, resulting in reduced actin binding, augments inhibition of Rap1-mediated integrin activity. This dynamic crosstalk has functional implications for cell morphology and integrin activity in cancer cells. In addition, SHANK3-actin interaction regulates dendritic spine morphology in neurons and autism-linked phenotypes *in vivo*.

Keywords: *SHANK3, actin, integrins, small GTPases, Rap1, integrin activation, molecular simulations, ASD*

Introduction

The distinct cell-types of a living organism can adopt remarkably versatile shapes that are dynamically regulated during physiological processes. Short-lived actin-rich cell protrusions such as filopodia, membrane ruffles and lamellipodia, as well as more stable structures such as dendritic spines, which mature from filopodia-like structures, are important contributors to cell shape and functionality[1,2]. In adherent cells, these structures receive input from several sources including regulators of the actin cytoskeleton, integrin-mediated cell-extracellular matrix interactions and small GTPase signaling[3–5]. Thus, crosstalk between these signals must be somehow carefully balanced within a cell.

SHANK3 is a scaffold protein predominantly studied in the post-synaptic density (PSD) of neurons. SHANK3 mutations and dysregulation are associated with autism spectrum disorders (ASD)[6–10], schizophrenia and Phelan-McDermid syndrome highlighting the importance of SHANK3 in neuronal development[6,8,11–13]. In the context of ASD, SHANK3 mutations contribute to disease pathogenesis through dysregulation of signaling and the actin cytoskeleton[2,8,14–16] and ASD symptoms of *Shank3*-deficient mice are alleviated by targeting actin regulators[16]. Thus, SHANK3-mediated regulation of actin dynamics is required for normal neuronal development and function. SHANK3 associates with different actin regulators including ABI1[17], Abp1[18,19], α-fodrin[20], SHARPIN[21], βPIX[22], CaMKKII[23,24], IRSp53[25], and cortactin[26,27], and SHANK3 mutations, identified in patients with ASD, impair SHANK3

association with actin in cells[28]. However, SHANK3 has not been reported to interact directly with actin, and the molecular mechanisms regulating the actin scaffolding functions of SHANK3 remain unknown. Moreover, whether SHANK3 regulates the actin cytoskeleton also in non-neuronal cells has not been investigated in detail.

SHANK3 is widely expressed outside of the central nervous system[29] with largely unknown functions. Our earlier unbiased RNAi screening in multiple cancer cell types and normal cells[29,30] revealed SHANK3 inhibition of integrin-mediated cell adhesion. The N-terminal SPN-domain of the protein adopts an unexpected Ras-association (RA) domain-like fold that binds and sequesters active Rap1 GTPase with high affinity, preventing recruitment of the integrin activator protein talin, and attenuating integrin function[29]. Two autism-linked SHANK3 patient mutations, R12C and L68P[8], are within the SHANK3 SPN-domain, and impair the ability of SHANK3 to bind to Rap1 and inhibit integrin activation[29], suggesting that SHANK3 could link small GTPases, integrins and regulation of the actin cytoskeleton. However, this has not been investigated.

Here, we present evidence of a novel, direct interaction between SHANK3 and actin, and demonstrate that the interaction is attenuated by an autoinhibited SHANK3 conformation. Moreover, we establish that SHANK3 mediates crosstalk between small GTPase signaling, regulation of the actin cytoskeleton and integrin activity in cells.

Results

The SHANK3 SPN-domain inhibits filopodia formation and colocalizes with actin

Filopodia are dynamic cell protrusions regulated by integrin activity and actin polymerization[31–33]. To gain insight into whether SHANK3 regulates these processes in non-neuronal cells, filopodia were induced by expressing the fluorescently tagged motor-protein myosin-X (MYO10) in U2OS osteosarcoma cells[33,34] and the dependence on integrin activity was validated by co-expressing known integrin activators, talin-1 and kindlin-2, which significantly increased the number of MYO10-positive filopodia (Figure S1A-B). Expression of full-length GFP-SHANK3 (functional domains highlighted in Figure 1A) reduced the number of MYO10-positive filopodia significantly (Figure 1B-C) and the effect was more prominent with isolated GFP-SHANK3 SPN-domain (referred to as GFP-SPN, Figure 1D-E), which interacts with active, GTP-bound Rap1, and is sufficient to inhibit integrins[29].

Unlike talin and kindlin[33], SHANK3 did not localize to filopodia tips (Figure S1C), suggesting an alternative mechanism of filopodia regulation, such as limiting the availability of Rap1-GTP or regulating the actin cytoskeleton. Surprisingly, GFP-SPN localized in filament-like structures proximal to the base of filopodia (Figure 1D) that overlapped with filamentous actin (F-actin) in U2OS (Figure 1F-G) and HEK293 cells (Figure S1D-E), implying SHANK3 SPN-domain recruitment to actin filaments in cells.

The SHANK3 SPN-domain binds F-actin directly

SHANK3 is a large scaffold protein interacting with many actin-associated and actin-binding proteins, including β-PIX[22], cortactin[26,27], ABI1[17], and Abp1[18,19] (Figure S1F). SHANK3 also associates with actin[28], but there are no previous reports of direct interaction between SHANK3 and actin, and it is unclear whether SHANK3 as such could regulate actin directly in addition to facilitating the recruitment of actin regulators to actin. To investigate this, we studied the localization of the SHANK3 SPN-domain and other SHANK3 fragments in U2OS cells stained for F-actin. While the SPN-domain (residues 1-92) colocalized with F-actin (Figure 1F-G, Figure S1D-E), similar localization was not observed with longer SHANK3 fragments (Figure S1G). In line with previous reports[35–37], these longer SHANK3 constructs lacking the C-terminus, displayed predominantly nuclear localization. The full-length SHANK3 localized throughout the cell and was not recruited to actin filaments (Figure S1G). This

indicates that the SPN-domain localizes to actin in a manner that is inhibited in the context of the full-length protein.

F-actin co-sedimentation assays with recombinant SPN protein demonstrated that GST-SPN interacts directly with purified F-actin (Figure S2A-B). However, the SPN-domain had no effect on F-actin disassembly in the presence and absence of cofilin-1 (Figure S2C-D). Thus, the SHANK3 SPN-domain interacts directly with actin filaments without altering their stability *in vitro*.

Identification of the SHANK3 SPN actin-binding site

The SHANK3 SPN-domain is structurally similar to the N-terminal F0-domains of talin[29,38] and kindlin-2 (Figure S2E-F) and the kindlin-2 F0-domain also binds actin directly[39]. Superimposition of the SHANK3 SPN-domain with the F0-domains of kindlin-1 and -2 revealed a corresponding spatial alignment between SPN residues Q37 and R38 and the kindlin F0 actin-binding residues L47 and K48 (Figure 2A-B). Furthermore, the local charge distribution of the predicted binding sites correlated well between kindlin F0- and the SHANK3 SPN-domain (Figure S2G). Thus, we hypothesized that Q37 and R38 residues in the SPN-domain may contribute to actin binding (Figure 2B). Replacing these residues with alanines (GFP-SPN-Q37A/R38A) significantly reduced the fraction of SPN overlapping with actin stress fibers (Figure 2C-D). Interestingly, the GFP-SPN-R12C mutant, with compromised Rap1-binding [29], overlapped with stress fibers similarly to WT SPN (Figure 2C-D), indicating that the interaction between the SPN-domain and Rap1 is not required for SPN recruitment to actin filaments in cells.

GFP-SPN-Q37A/R38A was also defective in pulling down β-actin from cell lysates when compared to GFP-SPN-WT or GFP-Cofilin-1 (positive control) (Figure 2E). Also, high-speed actin filament co-sedimentation assay suggests that GST-SPN-Q37A/R38A displays diminished binding to actin filaments compared to GST-SPN (Fig 2F-G, S2A, H). However, ~40 % of GST-SPN did not bind F-actin in this assay, suggesting that a fraction of recombinant GST-SPN was not fully active. Thus, the adjacent ARR domain may be required to stabilize the SPN fold and improve its functionality *in vitro*. Altogether, SHANK3 SPN-domain interacts with F-actin through a similar mechanism to kindlin-2 F0

domain, and consequently, the Q37A/R38A point mutant reduces SHANK3 SPN-domain binding to actin *in vitro* and in cells.

Crosstalk between SHANK3 SPN-actin binding and integrin inhibition

In light of our earlier study and the data provided here, it is evident that the SHANK3 SPN-domain can sequester active Rap1 to limit integrin activation[29], and bind actin directly. Therefore, we explored if these functions are coupled. The active-Rap1-binding interface of the SHANK3 SPN-domain (including the conserved, ASD-associated SPN R12 residue[29]) is distinct from the SPN actin-binding site (Q37/R38) (Figure 2H), suggesting that SHANK3 integrin inhibitory and actin-binding functions could be independent. To test this hypothesis, we assessed active integrin levels as a ratio of ligand-bound integrins over total cell-surface β1-integrins[29]. We have earlier shown that expression of GFP-SPN-WT, but not GFP-SPN-R12C (Rap1-binding defective mutant), reduces integrin activation[29]. Here, we observed that the actin-binding-deficient SPN-Q37A/R38A mutant inhibited soluble integrin ligand binding significantly and more potently than GFP-SPN-WT (Figure 2I). In adherent cells GFP-SPN-Q37A/R38A reduced active integrin levels (detected with 12G10 staining) significantly compared to control cells and more than SPN-WT (Figure S2I-J). Thus, reduced actin binding augments the integrin-inhibiting function of the SHANK3 SPN-domain, possibly due to increased availability of the SPN-domain to bind to plasma membrane-localized Rap1-GTP.

SPN-ARR fold opening dynamically regulates SPN–actin interaction

Many adhesion and actin-regulating proteins, such as talin, formins, ezrin-radixin-and-moesin (ERM) family proteins and N-WASP are autoinhibited by protein folding[40–43]. As there was no clear overlap between the SPN-ARR fragment or full-length SHANK3 with F-actin in cells (Figure S1G), we hypothesized that the conformation of SHANK3 may regulate its actin-binding function. In the published crystal structure, the SPN-ARR fragment of SHANK3[29] adopts a closed conformation that is mediated by intramolecular bonds between the SPN and ARR domains. Moreover, in full-length SHANK3 the closed conformation inhibits binding of α-fodrin, SHARPIN and exogenous SPN to the ARR-domain[44]. The SPN actin-binding residues Q37 and R38 are located proximal to the SPN-ARR domain interface[29,45], and may therefore be inaccessible for actin binding when the fold is in a closed

state. To test this hypothesis, we first analyzed recombinant SPN-ARR binding to F-actin. In contrast to the SPN-domain alone, recombinant SPN-ARR co-sedimented very inefficiently with filamentous β/γ-actin (Figure 3A, J).

Based on the SPN-ARR structure[29], we predicted that mutating N52 (personal communication, Prof. Igor Barsukov, University of Liverpool, UK) residue at the SPN-ARR interface, may destabilize the closed conformation (Figure 3B-C) and induce actin binding. Atomistic molecular dynamics (MD) simulations of the SPN-ARR-WT and N52R mutant indicated that this mutation would trigger a conformational change in the molecule, exposing the actin-binding site (Figure 3D-F). Based on the available structural data[29,45], we generated atomistic *in silico* models of the SPN-ARR region and modelled SPN-ARR-WT (System S1 in Table in the methods) and N52R mutant (System S2 in Table). Multiple independent 2 μs simulations of this model revealed dissociation and opening of the initially closed SPN-ARR interface in the N52R mutant (Figure 3D-F, Video S1), whereas the WT retained a closed conformation. Corroborating these findings, we used free-energy techniques to calculate the affinity of SPN-ARR binding to be $\sim\Delta G_{N52R}$=21 kJ/mol lower with the N52R mutant compared to the WT (Figure S3A, Systems S5 and S6 in Table). Likely, the charge repulsion between R52 (SPN-domain) and R179 (ARR-domain) plays a role in the decreased stability of the interface in the case of the N52R mutant, as no other differences were observed between WT and the N52R mutant in these simulations. These *in silico* data, indicating fold opening, were also supported by gel filtration experiments, which showed that while GST-SPN-ARR-WT eluted as a single peak, the N52R mutant eluted also earlier indicative of protein populations with more open conformation (Figure S3B-C). Moreover, SPN-ARR-N52R-mRFP protein, but not SPN-ARR-WT-mRFP, efficiently co-immunoprecipitated GFP-SPN in cells (Figure S3D-E), indicating that the N52R point mutation exposes the ARR-domain for subsequent binding to exogenous GFP-SPN. Whether the opening of the SPN-ARR fold additionally results in dimerization/oligomerization of the protein remains to be studied.

Whereas SPN-ARR-WT-mRFP displayed a diffuse cytoplasmic localization when expressed in U2OS cells, the SPN-ARR-N52R-mRFP mutant displayed striking localization to F-actin rich structures (Figure 3G-H). Moreover, co-sedimentation assay revealed that recombinant GST-SPN-ARR-N52R

protein binds β/γ-actin filaments with high affinity (apparent Kd of ~0.6 μM), whereas SPN-ARR-WT displays only very weak (undetectable) F-actin binding (Figure 3A, I-J). In addition, SPN-ARR-N52R-mRFP also pulled down β-actin from cell lysates as effectively as the positive actin-binding control mRuby-LifeAct (Figure S3F), whereas β-actin was largely absent from SPN-ARR-WT-mRFP pulldowns, again demonstrating that the N52R mutation opens the SPN-ARR interface to allow actin binding.

Active Rap1 competes with actin for SHANK3 binding

A recent study uncovered a second unconventional Rap1 binding site formed by both SPN and ARR domains[45]. In the simulations, Rap1 binding inhibited SPN-ARR N52R opening (Figure 3K-L, Video S2) and, experimentally, increasing the concentration of Rap1-GTP gradually decreased the proportion of GST-SPN-ARR-N52R (Figure 3M-N) and GST-SPN (Figure S3G-H) co-sedimenting with actin filaments *in vitro*. These data suggest that active Rap1-GTP and actin filaments compete for binding to the SPN-domain even though their binding sites on the SPN-domain are at least partially non-overlapping (Figure 2H, 3K) and can be independently disrupted by specific mutations. Imaging supported these data. Co-expression of active GFP-Rap1-Q63E with SPN-ARR-N52R-mRFP significantly reduced actin colocalization compared to cells co-transfected with GFP alone (Figure S3I-J). These data indicate that the SPN–actin interaction is regulated dynamically by the opening of the SPN-ARR fold and that Rap1 inhibits SHANK3-actin interaction via two mechanisms: by controlling the opening of the SPN-ARR interface and by competing with F-actin-binding to the SPN domain. We hypothesize that in cells, there is a physiological signal that triggers the opening of the SPN-ARR fold, but the nature of that signal remains to be investigated.

Open SPN-ARR fold interaction with actin requires the SPN actin-binding site

As the SPN-ARR N52R interacts with F-actin with higher affinity compared to the SPN-domain alone, we investigated the role of actin binding disrupting Q37A/R38A mutation in the context of the SPN-ARR N52R. While GFP-SPN-ARR-N52R exhibited marked overlap with F-actin, the triple mutant Q37A/R38A/N52R localized diffusely in the cytoplasm (Figure 4A-B). These findings were supported by actin co-sedimentation assays, where GST-tagged recombinant SPN-ARR-Q37A/R38A/N52R

exhibited reduced actin binding compared to SPN-ARR-N52R (Figure 3I-J, 4C-D). Because GST-fusion can induce dimerization of SPN-ARR, we also tested actin binding of monomeric maltose-binding protein (MBP) fusion proteins. MBP-SPN-ARR-N52R bound F-actin, although with slightly lower affinity compared to the GST-SPN-ARR-N52R (Figure S4A-B). This may be due to GST-mediated dimerization increasing the affinity of SPN-ARR N52R for F-actin, or MBP-fusion interfering with F-actin interaction or the opening of SPN-ARR N52R. Importantly, MBP-SPN-ARR-Q37A/R38A/N52R displayed severely reduced actin binding, Thus, residues Q37 and R38 in the SPN-domain are important for actin binding in the context of open SPN-ARR fold (Figure S4A-B).

The open SPN-ARR fold triggers full-length SHANK3 recruitment to actin filaments

To investigate the relevance of the SPN-ARR fold opening for SHANK3, we introduced the N52R point mutation into full-length GFP-SHANK3. Unlike GFP-SHANK3-WT and GFP-SHANK3-Q37A/R38A, GFP-SHANK3-N52R localized strongly to actin-rich structures (Figure 4E). Within stress fibers, GFP-SHANK3-N52R displayed a periodic localization pattern, interspersed with non-muscle myosin IIA staining (Figure 4F-G). Thus, also in the context of full-length SHANK3, the opening of the SPN-ARR interface (N52R mutation) activates the actin binding and SHANK3 recruitment to actin filaments in cells. However, as its localization across stress fibers is not as uniform as the GFP-SPN-WT (Figure 1F, 2C) or mRFP- and GFP-SPN-ARR-N52R (Figure 3G, 4A), we speculate that in the context of the full-length protein, interaction with SHANK3's other binding partners (Figure S1F) guides the actin-interaction to more specific actin structures. Similar to our observations with GFP-SPN-ARR-Q37A/R38A/N52R (Figure 4A-B), GFP-SHANK3-Q37A/R38A/N52R lost apparent overlap with actin-rich structures in cells (Figure 4H).

SHANK3-actin interaction modulates dendritic spine development

In neurons, SHANK3 localizes to actin-rich dendritic spines where it acts as a major scaffolding molecule for actin regulatory proteins[15,28]. *Shank3*-deficient mice have autism-like symptoms that can be rescued by restoration of *Shank3* in adult animals[46] or by targeting actin regulators[16]. To explore if the SHANK3 SPN-domain has a functional role in the development of dendritic spines, we expressed

GFP-SHANK3-WT and GFP-SPN-WT in primary hippocampal neurons isolated from WT rats. In mature neurons, consistent with previous reports, exogenous GFP-SHANK3-WT promoted the incidence of high spine density, albeit this did not reach statistical significance (Figure 5A)[28]. In contrast, the SPN-domain alone resulted in more neurons with medium or low spine density (Figure 5A, S5A) and mature GFP-SPN-WT-expressing neurons exhibited a significantly lower spine head diameter to neck length ratio compared to GFP-SHANK3-WT neurons (Figure 5B-C). These data indicate that expression of the SPN-domain alone has dominant-negative effects on spine density and morphology, most likely because it binds actin but lacks the binding domains for key PSD proteins such as AMPA receptors and actin-binding proteins such as IRSp53 and thereby fails to execute its "tethering" function. Thus, full-length or longer SHANK3 fragments are required for supporting normal spine development.

To investigate whether direct binding to actin is required for the functionality of full-length SHANK3, we expressed GFP-SHANK3-WT, and the actin-binding mutants GFP-SHANK3-Q37A/R38A and GFP-SHANK3-N52R first in primary WT rat neurons expressing endogenous SHANK3 (Figure 5D). Spine density did not change significantly in any of the conditions tested (Figure 5D-E). However, GFP-SHANK3-N52R-expressing neurons showed a striking 50 % decrease in the number of mushroom-shaped spines, and a large proportion (40 %) of spines had a stubby morphology and appeared stretched on the dendritic shaft (Figure 5D, F). Mature mushrooms were the major spine type in GFP-SHANK3-WT and Q37A/R38A-expressing neurons, and the proportion of other spine types was negligible (therefore numbers not included in Figure 5F). Despite their abnormal morphology, the dendritic clusters formed by GFP-SHANK3-N52R were positive for a presynaptic marker, the vesicular glutamate transporter (vGlut) (Figure S5B). Thus, the N52R mutant SHANK3 was localized at synaptic contacts and did not interfere with their formation. Instead, this mutant selectively altered the morphology of dendritic spines (Figure 5D-F, S5B), which is believed to be largely determined by their actin cytoskeleton[2,15,47]. These data indicate that the enhanced actin-binding activity of SHANK3 N52R interferes with proper actin network formation in maturing dendritic spines. Expression of GFP-SHANK3-Q37A/R38A did not lead to spines that differ significantly from WT SHANK3 expressing rat neurons, possibly due to the presence of endogenous SHANK3, given that SHANK3 homo-

oligomerizes in the PSD[48,49]. To overcome potential compensation by endogenous SHANK3, we expressed GFP-SHANK3-WT and Q37A/R38A in neurons isolated from *Shank3αβ*$^{-/-}$ mice that lack both the long α- and the shorter β-isoforms of *Shank3*[50,51]. Neurons re-expressing GFP-SHANK3-WT exhibited round spine heads, in keeping with earlier observations[28,37,44]. In contrast, GFP-SHANK3-Q37A/R38A-expressing neurons had lower spine density (Figure 5G) and significantly higher number of filopodia compared to the GFP-SHANK3-WT-expressing cells (Figure 5H-I) indicative of a developmental delay. These data suggest that the direct SHANK3-actin interaction is required for normal SHANK3 function in neurons and that the enhanced actin binding of the N52R mutant interferes with maturation of dendritic spines even in the presence of endogenous WT SHANK3.

SHANK3 actin-binding mutants are functionally defective in a zebrafish model of ASD

SHANK3 is well conserved in different species, and the zebrafish ortholog of human *SHANK3*, which exists in two copies (*shank3a* and *shank3b*), shares 55-68 % overall sequence homology with human *SHANK3*. Moreover, the sequence identity has been reported to be close to 100 % in many protein-encoding regions[52]. Transient morpholino-mediated knockdown of *shank3a* and *shank3b* expression or CRISPR/Cas9-mediated deletion of *shank3b* in zebrafish result in neurodevelopmental delay, including smaller brain, body and eye size, reduced eye pigmentation, as well as autism-like behavior such as repetitive swimming patterns, reduced locomotor activity and social interaction[11,52,53]. Therefore, we employed zebrafish embryos to address whether SHANK3-actin interaction plays a role in early neurodevelopment. Knockdown of *shank3b* with morpholinos significantly reduced eye pigmentation (Figure 6A-B) consistent with previous reports[53]. Introduction *of in vitro* transcribed GFP-SHANK3-WT mRNA significantly rescued eye pigmentation whereas GFP-SHANK3-N52R mRNA failed to rescue the phenotype (Figure 6B).

Next, we analyzed zebrafish embryos in a motility assay (Figure 6C-D). As mRNA rescue works most efficiently in early time points, we used 2 days post-fertilization embryos and utilized pentylenetetrazole (PTZ) to induce zebrafish embryo motility[54]. *shank3* knockdown resulted in reduced swim distance (Figure 6D). Introduction of WT rat GFP-SHANK3 mRNA rescued the effects on swim distance, but

both GFP-SHANK3 mRNAs carrying N52R or Q37A/R38A mutations failed to rescue this phenotype (Figure 6D). These results suggest that mutations that either impair or enhance the actin binding function of SHANK3 have loss-of-function effects on established SHANK3 regulated phenotypes *in vivo*.

Discussion

Here, we uncover a direct interaction between SHANK3 and actin, driven by a SHANK3 conformational switch that is inhibited by Rap1, and reveal a cellular role for SHANK3 actin-binding. The SHANK3-SPN-domain binds to active Rap1 and in doing so, inhibits an important integrin activation pathway[27]. Our data suggest that dynamic regulation of the N-terminal SPN-ARR conformation by active Rap1 and other, yet unknown signals, are important for SHANK3 to coordinate crosstalk between integrin activity and the actin cytoskeleton. A plausible scenario would be that when active Rap1 is highly abundant, SHANK3 binds to Rap1 sequestering it from the integrin activating Rap1-talin axis, and the 'closed' SHANK3 conformation becomes stabilized. However, in areas of active actin polymerization, actin filaments and additional signals that facilitate the conformational switch, 'open' SHANK3. This favors actin binding and Rap1 is released promoting integrin activation. Thus, SHANK3 may play a key role in ensuring that Rap1-mediated integrin activation is restricted to actin-rich regions of the cell.

Understanding how the passage of information from adhesions to the actin cytoskeleton and back is mediated in a dynamic cell requires detailed understanding of the players involved. The Rap1 GTPase promotes activation of integrins[32,55,56], and integrin-mediated cell adhesion sequentially activates Rac and RhoA GTPases to induce actin polymerization, cell spreading and generation of stress fibers[57,58]. Meanwhile, actin and actin-binding proteins, such as talin, support integrin activity, receptor clustering and adhesion maturation[59,60]. Therefore, coordination of integrin function and actin dynamics is expected to play a central role in the regulation of cell morphology and dynamics. However, there are limited examples of proteins linking actin and integrin function, especially in the context of integrin inactivation, specific adhesion types and actin-rich cell processes. The ability of SHANK3 to interact directly with F-actin through its N-terminal SPN-domain, suggests SHANK3 is an important node

connecting the dynamic regulation of the actin cytoskeleton with Rap1-mediated integrin activity. It is important to note that whereas the isolated SPN-domain displayed a moderate affinity to actin filaments *in vitro*, the 'activated' SPN-ARR fragment of SHANK3 binds F-actin with high affinity (Figures 2G, 3J, 4D, S4B). Thus, the recombinant SPN-domain may be partially inactive *in vitro*, the adjacent ARR domain may help stabilizing its fold, or the ARR-domain may also contribute to F-actin binding by SHANK3.

SHANK3 expression promotes actin polymerization and increases F-actin levels in dendritic spines. This has been largely attributed to the ability of SHANK3 to recruit different actin regulators to the PSD. The interaction of the SHANK3 SPN-domain with actin did not seem to modulate actin dynamics directly. In contrast, enhanced and diminished actin interaction of full-length SHANK3 affected dendritic spine morphology. Thus, it is plausible that the main function of SHANK3-actin interaction is to coordinate integrin activation with the actin cytoskeleton, and to recruit SHANK3-associated actin regulators to actin filaments. However, as these SHANK3 actin-binding mutants retain their canonical Rap1-binding site, we cannot draw any conclusions regarding their influence on Rap1 signaling in dendritic spines.

The N-terminal SPN-ARR is folded in a closed conformation *in vitro*[29,44]. This fold has been shown to inhibit the binding of SHANK3-interacting proteins SHARPIN and α-fodrin to the ARR-domain[44] and we find that the closed SPN-ARR does not interact with actin. Furthermore, atomistic simulations indicate that this closed conformation is stabilized by Rap1 binding. Collectively, these data suggest that the SPN-ARR fold opening and actin binding are dynamically regulated by Rap1 activity. Unlike the SPN-domain alone, full-length SHANK3 is not specifically recruited to stress fibers in cells. Thus, we hypothesize that in cells, a physiological signal, such as post-translational modification (PTM), co-factor recruitment, or interaction with membrane lipids, triggers the opening of the fold and presumably spatially controls SHANK3-actin interaction. For example, the interaction between SHANK3 and ABI1 is regulated by phosphorylation at S685, a residue in the PP-domain, and an ASD-linked patient mutation S685I interferes with this phosphorylation abolishing interaction with ABI1 and decreasing downstream actin polymerization[17]. However, we have thus far failed to obtain evidence supportive of

phosphorylation-mediated regulation of SHANK3 recruitment to actin filaments in cells and the identity of the signal(s) regulating the SPN-ARR fold opening remains to be determined.

Other proteins have previously been shown to regulate integrin activity and bind actin. These include well-established integrin activators talin and kindlin[59]. These proteins are, however, activators not inhibitors of integrins and actin binding does not directly affect their integrin activation properties. SHANK3 is unique in that its ability to inhibit integrin activity is coupled directly to actin binding. This would enable it to locally co-ordinate Rap1-signaling and integrin activity in response to changes in actin polymerization and vice versa. Given the relevance of SHANK3 function in human health, SHANK3 is a prime candidate to fine-tune numerous physiological processes from neuronal actin regulation to cell migration in multiple other tissues. In this respect, dissection of the mechanisms regulating SHANK3 in physiology and pathology is a major challenge ahead of us.

Acknowledgements

We thank the Cell Imaging and Cytometry and the Zebrafish Core facilities (Turku Bioscience Centre, University of Turku and Åbo Akademi University) and University of Turku Central Animal Laboratory all supported by Biocenter Finland for services in imaging and animal experiments. CSC – IT Center for Science Ltd is acknowledged for computing resources. We thank P. Laasola, J. Siivonen and V. Pollari for technical help and H. Hamidi for editing of the manuscript and illustrations. I. Barsukov, J. Pouwels, P. Hotulainen and the Ivaska lab are acknowledged for important suggestions, feedback and stimulating discussions. This study has been supported by an ERC CoG grant 615258 (J.I.), the Academy of Finland (J.I., G.J. E.T.C., P.L., I.V.), the Finnish Cancer Foundation (J.I., P.L., I.V.), the Sigrid Juselius Foundation (J.I., G.J., I.V.) and by grants from Deutscher Akademischer Austauschdienst (DAAD; to F.H.N.), Deutsche Forschungsgemeinschaft (DFG; KR 1321/9-1; to H.-J.K.), and the Human Frontier Science Program (project no. RGP0059/2019 to I.V.). S.I.S. has been supported by the Svenska kulturfonden, Finnish Cultural Foundation, University of Turku Foundation and Maud Kuistila Memorial Foundation. S.I.S. and M.M. have been supported by University of Turku

Drug Research Doctoral Programme, J.L. by Turku Doctoral Programme of Molecular Medicine and A.I. by Turku Doctoral Programme of Molecular Life Sciences.

Author contributions

Conceptualization, S.I.S., J.L., G.J., I.V., P.L., and J.I.; Methodology, S.I.S., E.K., M.M., J.V., G.J., J.L., F.H.N., I.P. and J.I.; Formal Analysis, S.I.S., E.K., K.K., A.I., L.A., J.V., J.L., P.H., F.H.N, I.P. and J.I.; Investigation, S.I.S., E.K., K.K., J.L., J.V. P.H., F.H.N., G.J., M.M., I.P. and J.I.; Writing – Original Draft, S.I.S. and J.I.; Writing – Review and Editing, S.I.S., H.J.K., P.L., J.V., I.V., M.M., E.T.C. and J.I.; Supervision, H.J.K., I.V., E.T.C., P.L., and J.I.; Funding Acquisition, H.J.K., P. L., E.T.C., I.V., and J.I.

Declaration of interests

Authors declare no competing interests.

Main figure titles and legends

Figure 1. The SHANK3 SPN-domain inhibits MYO10-positive filopodia formation and colocalizes with F-actin. A, Schematic of SHANK3 functional domains. SPN, Shank/ProSAP N-terminal domain; ARR, ankyrin repeat region; SH3, Src homology 3 domain; PDZ, PSD-95/Discs large/ZO-1 domain; PP, proline-rich region; SAM, sterile alpha motif domain. SPN-domain interactors are indicated. **B-E,** Filopodia formation in U2OS cells co-expressing GFP control, GFP-SHANK3 (B-C) or GFP-SPN (D-E) together with MYO10-mCherry and plated on fibronectin for 2 h. Representative bottom plane confocal images (B, D) and quantification of filopodia numbers (C, E) are shown. **F, G,** F-actin (phalloidin-647) and GFP localization in U2OS cells expressing either GFP control or GFP-SPN and plated on fibronectin (3-4 h). Representative bottom plane confocal images (F) and quantification using the coloc2 ImageJ plugin (G) are shown. Orange squares highlight regions of interest (ROI), which are magnified. All representative images and data are from n = three independent experiments. Data are mean ± standard deviation (s.d.) (C, E) or presented as Tukey box plots with median and the interquartile range (IQR) (whiskers extend to 1.5x the IQR and outliers are displayed as individual points). Statistical analyses: (C, E) Mann-Whitney two-tailed T-test. (G) Kruskal-Wallis non-parametric test and Dunn's multiple comparisons post hoc test. Number of cells

analyzed: (C) 74 (GFP ctrl) and 67 (GFP-SHANK3-WT). (E) 41 (GFP ctrl) and 43 (GFP-SPN). (G) 79 (GFP ctrl) and 84 (GFP-SPN). See also Figure S1.

Figure 2. The SHANK3 SPN-actin interaction is inhibited by mutation of the predicted actin-binding site. A, Superimposition of the SHANK3 SPN-domain and the kindlin-1 F0 domain using Pymol (PDB codes: 5G4X, 2KMC). **B,** SHANK3 SPN-domain structure with the putative actin-binding residues Q37/R38 highlighted. **C, D,** F-actin (phalloidin-647) and GFP colocalization in U2OS cells expressing GFP control or GFP-tagged SPN-WT, Q37A/R38A or R12C and plated on fibronectin (3-4 h). Representative bottom plane confocal images (C) and quantification (D) using the coloc2 ImageJ plugin are shown. Pink-colored boxes have been shown earlier in Figure 1G. **E,** GFP-trap pulldowns in U2OS cells expressing GFP control (negative control), GFP-Cofilin-1 (positive control), GFP-SPN-WT or Q37A/R38A. Input lysates and immunoprecipitated (IP) samples were analyzed using β-actin and GFP antibodies as indicated. **F, G,** GST-SPN-WT (1 μM) or Q37A/R38A (1 μM) interaction with β/γ-actin filaments in high-speed (60.000 rpm) co-sedimentation assays. A representative experiment (F) and quantification (G) of co-sedimenting SPN-WT and Q37A/R38A against actin are shown. At high concentrations the amount of co-sedimenting GST-SPN plateaued at ~0.60 μM, indicating that ~40 % of GST-SPN was inactive and unable to bind actin filaments. S, supernatant fraction; P, pellet fraction. **H,** SHANK3 SPN-domain with the Rap1-binding residue R12 and actin-binding residues Q37 and R38 highlighted. **I,** Flow cytometry analysis of integrin activity (fibronectin fragment 7-10 binding relative to total cell-surface α5β1-integrin) in CHO cells expressing GFP-SPN-WT or SPN-Q37A/R38A compared to GFP control. All representative micrographs, immunoblots and data are from n = three independent experiments. Data are presented as Tukey box plots (D), as exponential curve with standard deviation (G) or as mean ± s.d. (I). Statistical analyses: (D) Kruskal-Wallis non-parametric test and Dunn's multiple comparisons post hoc test and (I) Welch's t-test with subsequent Bonferroni correction. Number of cells analyzed: (D) 57 (GFP ctrl), 88 (GFP-SPN-WT), 90 (Q37A/R38A) and 68 (R12C). See also Figure S2.

Figure 3. Mutation of the SHANK3 SPN-ARR interface induces an open conformation and promotes actin binding. A, GST-SPN-ARR (1 μM) binding to β/γ-actin filaments (0, 2, 4, 6, 8 and 12 μM) in high-speed co-sedimentation assay. A representative experiment is shown. **B, C,** Visualization of the SHANK3 SPN-ARR (5G4X, residues 1-348) fold and the close proximity of residues Q37/R38 to the ARR-SPN interface. **D, E,** The structure of SPN-ARR WT (D) and N52R mutant (E) determined from MD simulations at 1000 ns. The

snapshots are taken from Systems S1 and S2 (see Table). **F,** Analysis of the distance between Cα atoms of residues N52 and R179 during the simulations. R179 was selected as it is located directly next to the N52 residue in both available X-ray structures (5G4X and 6KYK). The data are calculated from Systems S1 and S2 (Table). Standard errors are represented with shading. **G, H,** U2OS cells expressing RFP control, SPN-ARR-WT-mRFP or SPN-ARR-N52R-mRFP, plated on fibronectin (3-4 h) and stained for F-actin (phalloidin-647). Representative bottom plane confocal images (G) and Pearson's correlation coefficient (H) quantified using coloc2 ImageJ plugin are shown. Two independent experiments. **I, J,** GST-SPN-ARR-N52R (1 µM) binding to β/γ-actin filaments (0, 2, 4, 6, 8 and 12 µM) in a high-speed co-sedimentation assay (I) and quantification of GST-SPN-ARR-WT (representative gel presented in panel A) and SPN-ARR-N52R (J). The apparent kD values are 0.6 µM for GST-SPN-ARR-N52R, and non-detectable for GST-SPN-ARR-WT. **K,** The structure of SPN-ARR-N52R with two Rap1-GTP molecules taken from MD simulations (System S4, Table) at 1000 ns. **L,** Analysis of the distance between the Cα atoms of residues R179 and R52 as a function of simulation time. The data are calculated from Systems S3 (Table). **M, N,** Analysis of GST-SPN-ARR-N52R (1 µM) interaction with β/γ-actin filaments (2 µM) in the presence of active GMPPCP-loaded (GTP-analogue) His-Rap1b (0, 0.5, 1, 2, 4, 6 and 8 µM). A representative high-speed co-sedimentation experiment (M) and quantification (N). Standard errors are represented with shading. All data are from three independent experiments unless otherwise indicated. Data represent mean ± s.d. (H, J and N). Number of cells: (H) 57 (RFP ctrl), 52 (SPN-ARR-WT-mRFP) and 53 (SPN-ARR-N52R-mRFP). Statistical analysis: (H) Kruskal-Wallis non-parametric test and Dunn's multiple comparisons post hoc test. S, supernatant fraction; P, pellet fraction. See also Figure S4, Videos S1, S2 and Table.

Figure 4. The SHANK3 N52R mutant localizes to actin stress fibers. A, B, U2OS cells expressing GFP-SPN-ARR WT, SPN-ARR N52R or SPN-ARR Q37A/R38A/N52R plated on fibronectin (3-4 h) and stained for F-actin (phalloidin-647). Representative bottom plane confocal images (A) and Pearson's correlation coefficient B) for F-actin and GFP quantified using coloc2 ImageJ plugin are shown. Three independent experiments. **C, D,** GST- SPN-ARR-WT (1 µM), SPN-ARR-N52R (1 µM) and SPN-ARR-Q37A/R38A/N52R (1 µM) binding to β/γ-actin filaments (0, 2, 4, 6, 8 and 12 µM) in a high-speed co-sedimentation assay (C) and quantification (D). Representative gels and quantifications for WT and N52R are also shown in 3A, I-J. The apparent kD values are 0.6 µM for GST-SPN-ARR-N52R, 2.9 µM for GST-SPN-ARR-Q37A/R38A/N52R and non-detectable for GST-SPN-ARR-WT. **E,** Representative bottom plane confocal images of U2OS cells expressing GFP-SHANK3-WT,

Q37A/R38A or N52R plated fibronectin (3-4 h) and stained for F-actin (attophalloidin-647). **F, G,** Distribution of GFP-SHANK3-N52R and endogenous NMIIA (non-muscle myosin IIA) along stress fibers in U2OS cells plated on fibronectin (3-4 h). Representative bottom plane confocal images (F) and a representative line scan along an actin stress fiber (G) are shown. Orange squares highlight ROI that are magnified. All data are from three independent experiments unless otherwise indicated. Data represent mean ± s.d. (B, D). Number of cells: (B) 40 (GFP-SPN-ARR-WT), 48 (GFP-SPN-ARR-N52R) and 50 (GFP-SPN-ARR-Q37A/R38A). Statistical analysis: (B) Kruskal-Wallis non-parametric test and Dunn's multiple comparisons post hoc test. S, supernatant fraction; P, pellet fraction. See also Figure S4.

Figure 5. SHANK3-actin interaction regulates spine morphology and number. A, Quantification of spine density of WT primary rat hippocampal neurons fixed at DIV16-18. **B, C,** Representative maximum intensity projection confocal images (B) of WT primary rat hippocampal neurons fixed at DIV16-18 co-expressing RFP and GFP control, GFP-SHANK3-WT or GFP-SPN and (C) quantification of spine head diameter to neck length ratio. **D, E, F,** Analysis of WT primary rat hippocampal neurons expressing GFP-SHANK3-WT, Q37A/R38A or N52R fixed at DIV16. Representative maximum intensity projection confocal images (D) and quantification of spine density (C) and number of different spine types per 20 µm dendrite (E) are shown. The neurons were stained with the dendritic marker MAP2 (microtubule-associated protein 2). Orange arrow highlights thin spines and blue arrows highlight stubby spines. **G, H, I,** Analysis of spine development and filopodia formation in primary *Shank3αβ*$^{-/-}$ mouse hippocampal neurons fixed at DIV14 expressing GFP-SHANK3-WT or Q37A/R38A. Quantification of spine density (E), filopodia density (F) and proportion of filopodia (G) are shown. (A) Data represent the proportion of neurons in each spine density category. (C-G) Data represent mean ± s.d.; (A) n = 14 (GFP ctrl), 13 (GFP-SHANK3-WT) and 25 (GFP-SPN-WT) neurons; (C) 14 neurons, 154 spines (GFP ctrl), 16 neurons, 223 spines (GFP-SHANK3-WT) and 7 neurons, 104 spines (GFP-SPN-WT); (E, F) number of branches: 45 from 15 neurons; (G, H, I) Number of secondary dendrites: 39 (WT) and 45 (Q37A/R38A). Statistical analysis: (A) Chi-Square. (C) one-way ANOVA. (E, F) Kruskal-Wallis non-parametric test and Dunn's multiple comparisons post hoc test. (E, F, G) Mann-Whitney two-tailed T-test. See also Figure S5.

Figure 6. Dynamic SHANK3-actin binding is necessary for rescue of autism-linked phenotypes *in vivo.* A, B, Eye pigmentation phenotype in zebrafish embryos microinjected with a *shank3b*-targeting morpholino (MO) and rescued with *in vitro* transcribed *SHANK3*

mRNA co-injections. Images of the head of zebrafish embryos (A) and quantification of the pigmentation of the eye (30 hpf) (B) are shown. **C, D,** Motility of zebrafish embryos microinjected with *shank3a and b*-targeting morpholinos and rescued with *SHANK3* mRNA co-injections. Motility was analysed before and after 20 mM pentylenetetrazole (PTZ) addition. Zebrafish embryos were imaged at high-speed 30 fps and tracked automatically using Ethovision XT software. Recorded tracks of zebrafish embryo movement (C) are displayed in magenta and overlaid on the image of the 96-well plate. The total swimming distance (mm) of zebrafish embryos (D) is also shown.

Number of embryos: (B) Control MO + GFP (37), *shank3b* MO + GFP (12), *shank3b* MO + N52R (17), *shank3a+b* MO + WT (22), uninjected (10). (D) (unstimulated/PTZ stimulated), Control MO + GFP (58 / 60), *shank3a*+b MO + GFP (16 / 17), *shank3a+b* MO + N52R (22 / 25), *shank3a+b* MO + Q37A/R38A (28 / 33), *shank3a+b* MO + WT (25 / 25), uninjected (24 / 24). Data are mean ± s.d. Statistical analysis: (B) non-parametric Kruskal-Wallis test and Dunn´s post-hoc test. (D) Rout´s outlier detection algorithm (Q=0.5%) followed by non-parametric Kruskal-Wallis test and Dunn´s post-hoc test.

STAR METHODS

Resource Availability

Contact for Reagent and Resource Sharing

Further information and requests for resources and reagents should be directed to and will be fulfilled by the Lead Contact, Johanna Ivaska (johanna.ivaska@utu.fi).

Materials Availability

Newly generated SHANK3 full-length, SPN and SPN-ARR plasmids are available from the authors upon request. No other unique reagents were generated in this study.

Data and Code Availability

The published article includes all data generated or analyzed during this study. Parameters for the simulations are described in the methods.

Experimental Model and Subject Details

Cell lines

CHO (Chinese hamster ovary) cells were grown in α-MEM medium (Sigma-Aldrich) supplemented with 5 % fetal bovine serum (FBS, Gibco), 2 mM L-glutamine (Sigma-Aldrich) and 1 % (vol/vol) penicillin/streptomycin (pen/strep, Sigma-Aldrich). HEK293 (human embryonic kidney) and U2OS (human bone osteosarcoma) cells were maintained in Dulbecco's modified Eagle's medium (DMEM, Sigma-Aldrich) supplemented with 10 % FBS, 2 mM glutamine and 1 % pen/strep. All cell lines were regularly checked for mycoplasma contamination.

Primary murine and rat neurons were isolated as described in the methods and cultured on 0.1 mg/ml poly-L-lysine-coated glass coverslips in the presence of either Neurobasal-A medium (Thermo Fisher Scientific) supplemented with 2 mM glutamine, 50 U/ml penicillin, 50 µM streptomycin and B27 Neuronal supplement (Gibco, Thermo Fisher Scientific) or Neurobasal medium supplemented with 2 % B27 Neuronal Supplement, 1 % GlutaMAX and 1 % pen/strep.

Animal models

Sprague-Dawley rats and Wistar Unilever outbred rats (strain HsdCpb:WU) (Envigo, Horst, The Netherlands) were used for isolation of primary hippocampal neurons. *Shank3 αβ*-deficient mice were provided by Tobias Boeckers (Univ. of Ulm, Germany)[50].

Timed, pregnant animals were housed in individual cages, with access to food and water ad libitum. All animal experiments were approved by, and conducted in accordance with, the Turku Central Animal Laboratory regulations and followed national guidelines for Finnish animal welfare, or regulations of the Animal Welfare Committee of the University Medical Center (Hamburg, Germany) under permission number Org766.

Wild-type (AB strain) zebrafish were housed under license MMM/465/712-93 (issued by the Ministry of Agriculture and Forestry, Finland) and embryos were obtained via natural mating.

Methods Details

Isolation and culture of primary hippocampal neurons

Newborn Sprague-Dawley rats were decapitated and their hippocampus was placed into dissection media (1 M Na_2SO_4, 0.5 M K_2SO_4, 1 M $MgCl_2$, 100 mM $CaCl_2$, 1 M Hepes (pH 7.4), 2.5 M Glucose, 0.5 % Phenol Red). Meninges were removed and hippocampal pieces were collected into dissection media containing 10 % KyMg, followed by washing. Hippocampal tissue was then incubated with 10 U/ml papain (#3119, Worthington) for 15 min at 37ºC, repeated two times. Papain was inactivated by incubation with 10 mg/ml trypsin inhibitor (Sigma, T9128) for 2 x 5 min at 37ºC. Hippocampal tissue was then homogenized by gentle pipetting. Cultures were plated on 0.1 mg/ml poly-D-lysine-coated glass coverslips and maintained in Neurobasal-A medium (Thermo Fisher Scientific) supplemented with 2 mM glutamine, 50 U/ml penicillin, 50 µM streptomycin and B27 Neuronal supplement (Gibco, Thermo Fisher Scientific).

Pregnant Wistar rats (Envigo; 4-5 months old) were sacrificed on day E18 of pregnancy using CO_2 anesthesia, followed by decapitation. Neurons were prepared from all embryos present, regardless of gender (14-16 embryos). The hippocampal tissue was dissected, and hippocampal neurons were extracted by enzymatic digestion with trypsin, followed by mechanical dissociation. Cells were grown

in Neurobasal medium supplemented with 2 % B27 Neuronal Supplement, 1 % GlutaMAX and 1 % pen/strep (Gibco, Thermo Fisher Scientific) on 0.1 mg/ml poly-L-lysine-coated glass coverslips. Neurons were transfected using the calcium phosphate method as described below. Neurons from *Shank3 αβ*-deficient mice were isolated and transfected in a similar manner, except that the pregnant mice were sacrificed at E17 and neurons were analyzed at DIV 14 since *Shank3 αβ*$^{-/-}$ neuron cultures are more fragile *in vitro*.

Plasmids

The SHANK3-mRFP (pmRFP-N3, Clontech) was described earlier[29], and deletion constructs generated either by using appropriate restriction sites or PCR amplification of cDNA fragments prepared in pmRFP-N3 vectors[62]. The tD-tomato-N1 vector was obtained from Clontech. The construct coding for a GFP-fusion of the SHANK3 SPN domain has been described previously[29,44]. A construct coding for N-terminal GFP-tagged full-length rat SHANK3 in the pHAGE vector was obtained from Alex Shcheglovitov (Univ. of Utah, Salt Lake City)[29,62]. Constitutively active human Rap1A (pEGFP-C3-Rap1Q63E, here referred to as GFP Rap1 Q63E) was a gift from B. Baum and S. Royle[63,64]. Myo10-mCherry was a gift from S. Strömblad, kindlin-2-GFP from M. Parsons and GFP-talin-1 from B. Goult. mRuby-Lifeact was obtained from Addgene (#54560). pEGFP-C1 and mRFP-N1 were used as controls in this study.

For bacterial expression as glutathione-S-transferase (GST) fusion proteins, parts of the rat SHANK3 cDNA were amplified by PCR with oligonucleotide primers carrying appropriate restriction sites. Amplified fragments were subcloned into pGEX-2T or pGEX4T2 vectors (GE Healthcare) in frame with the GST coding sequence.

Different point mutations were introduced into SHANK3 constructs by site-directed mutagenesis (Gene Universal) or by using mutagenic oligonucleotides and the QuikChange II site-directed mutagenesis kit (Agilent) according to the manufacturer's instructions. Maltose-binding protein (MBP)-tagged fusion plasmids were obtained by transferring the SHANK3 cDNAs (WT and mutants) to pCoofy4 a gift from Sabine Suppmann (Max Planck Institute for Biochemistry, Germany) by utilizing restriction free cloning method with NEBuilder cloning kit (NEB, cat. #E5520S).

N-terminally EGFP-tagged SPN-ARR plasmids (WT, N52R, Q37A/R38A/N52R) were generated by amplifying the SPN-ARR fragments from full-length plasmids already harbouring these mutations. By using PCR primers (5'-attagagaattctgggtcgaccatggacg and 5'-attagaggtaccttattccctgaatggtacgacatccga), the amplified fragments were then inserted between EcoRI and KpnI restriction sites in a EGFP-C1 plasmid (Clontech). All used restriction enzymes were obtained from New England Biolabs. All modified plasmids were verified by sequencing before use.

Transient transfections

Plasmids were transiently transfected into CHO, HEK293, and U2OS cells using Lipofectamine 3000 and P3000™ Enhancer Reagent (Thermo Fisher Scientific Inc, # L3000-015) according to manufacturer's instructions. Cells were cultured for 24 h before they were re-plated (plating times indicated in figure legends) in subsequent experiments.

Primary neurons were either transfected at DIV16 with Lipofectamine™ 2000 Transfection Reagent (Thermo Fisher Scientific Inc, #11668019) according to manufacturer's instructions, or using the calcium phosphate method at DIV7-9. For the latter, the complete Neurobasal medium was collected from wells one hour before transfection and replaced with pre-warmed transfection medium (MEM+GlutaMAX). Plasmid DNA was diluted in H_2O and mixed with 2.5 M $CaCl_2$. An equal amount of 2X Hepes buffered salt solution (HBS) was added drop-wise to the reaction tube under continuous mixing. The reaction was incubated at room temperature (RT) for 30 min and then divided between the wells of the cell culture plate. After a 2 h incubation with the transfection mixture, the cells were washed seven times with 1×Hank's Balanced Salt Solution (HBSS). After the final wash, the previously collected Neurobasal medium was added back to the cells. 2xHBS: NaCl 274 mM; KCl 10 mM; Na_2HPO_4 1.4 mM; D-Glucose 15 mM; Hepes 42 mM; adjusted to pH 7.05 with NaOH.

Immunofluorescence, microscopy and image analysis

For the immunofluorescence experiments with cell lines, 35 mm #1.5 glass-bottom dishes (Cellvis, #D35-14-1.5-N) were coated with bovine plasma fibronectin (Merck-Millipore, #341631, diluted to 10 µg/ml in PBS) overnight at +4 °C. Cells were plated on dishes in the appropriate medium for the indicated times. Cells were then fixed and permeabilized simultaneously by adding 16 % (wt/vol) paraformaldehyde and 10 % (vol/vol) Triton-X directly into the media at a final concentration of 4 %

PFA and 0.1-0.25 % (vol/vol) Triton-X for 5-10 min, after which samples were washed with PBS and quenched with 1 M glycine in PBS for 25 min. Samples were incubated with primary antibodies (30 min at RT), followed by washes and incubation with fluorescently-conjugated secondary antibodies for 30 min at RT. Unless otherwise stated, the bottom plane was imaged with a Marianas spinning disk confocal microscope (3iw1) equipped with a CSU-W1 scanner (Yokogawa) and Hamamatsu sCMOS Orca Flash 4.0 camera (Hamamatsu Photonics K.K.) using a 63x/NA 1.4 oil, Plan-Apochromat, M27 with DIC III Prism objective. For images acquired using the structured illumination microscope (SIM), cells were plated on high tolerance glass-bottom dishes (MatTek Corporation, coverslip #1.7). Samples were fixed, permeabilized and stained as described above. Just before imaging, samples were washed three times in PBS and mounted in vectashield (Vector Laboratories). The SIM used was DeltaVision OMX v4 (GE Healthcare Life Sciences) fitted with a 60x Plan-Apochromat objective lens, 1.42 NA (immersion oil RI of 1.516) used in SIM illumination mode (five phases x three rotations). Emitted light was collected on a front-illuminated pco.edge sCMOS (pixel size 6.5 mm, readout speed 95 MHz; PCO AG) controlled by SoftWorx.

Primary neurons were grown on glass coverslips and fixed at indicated DIV with 4 % PFA followed by permeabilization with 0.1-0.5 % Triton-X and blocking with 10 % horse serum in PBS. Neuron samples were stained as described above and imaged either with an LSM880 Airyscan laser-scanning confocal microscope (Zeiss) with Airyscan detector using 63x/ 1.4 oil objective, or with a Leica TCS SP5 confocal microscope with 63x/1.4-0.60 HCX PL APO Lbd. Bl. oil objective.

Quantitative image analysis was performed with Fiji/ImageJ and Neurolucida Explorer (analysis of dendritic spines described below). Colocalization analysis was done with ImageJ coloc2 plugin.

Analysis of dendritic spines

For dendritic spine head-and-neck ratio measurements, ImageJ's line measurement tool was used on maximum intensity projection images and at least 16 spines were selected randomly from each cell. For neck length, a line was drawn and distance was measured from the base of the neck to the stem of the spine head. Head diameter was estimated by measuring the distance of a line between the two most distant points on the spine head. Head diameter/neck length ratios were calculated accordingly using

Microsoft Excel. Spine density was analysed from Z-stacks using Neurolucida Explorer (MBF Bioscience, Williston, DC, USA) or with ImageJ. In *Shank3αβ*$^{-/-}$ neurons, filopodia and other spine types were categorised manually on the basis of morphology of spines and filling with tdTomato and F-actin dye observing whether they had a visible neck and a separate bulbous head (spine) or no apparent head at all (filopodia). General scoring of neurons with high, medium and low spine density was done similarly based on visual observation and manually dividing neurons into these categories based on their appearance – whether they had typical, high spine density, very low number of spines or some spine development, but less than expected (medium).

Expression and purification of recombinant proteins

Competent E. coli BL21 bacteria were transformed with expression constructs having either GST- or His- MBP-tag (also includes a His-tag) and grown in LB medium (for GST SPN) or autoinduction media (for GST and MBP SPN-ARR) supplemented with selection antibiotics (ampicillin or kanamycin), at 37°C until an OD600 of 0.6-0.8. In case of GST SPN, protein production was induced by the addition of 0.1 mM IPTG overnight at 18 °C, while for GST- and MBP SPN-ARR constructs grown in autoinduction media, culture was continued at 22 °C for 24h. The next day, the bacterial pellet was harvested by centrifugation for 20 min at 6000 g and then resuspended in cold lysis buffer (50 mM Tris, 150-300 mM NaCl, cOmplete™ protease inhibitor tablet (Roche, #5056489001) and 2 µl/ml DNAse (Sigma-Aldrich, #11284932001)). A small spoonful of lysozyme from chicken egg white (Sigma-Aldrich, #L6876-5G) were added to lyse the bacteria for 30 min at 4 ºC with gentle rotation. To complete the lysis, 1 % Triton-X and 1x BugBuster (Merck Millipore, #70584-4) was added to GST SPN proteins together with lysozyme, whereas GST and MBP SPN-ARR where sonicated 4 x 1 min on ice. The lysate was cleared by centrifugation at 15000-18000 g for 1 h at 4 °C. The cleared lysate was incubated with either Glutathione Sepharose® 4B (for GST-tagged proteins, GE Healthcare, #17-0756-01) or Protino Ni-TED resin (for MBP-tagged proteins, Macherey-Nagel, #745200.5) for 1 h at 4 °C with rotation and then transferred to gravity columns (Talon® 2 ml Disposable Gravity Column, Clontech, #635606-CLI). The lysate was drained and the beads were washed five times with cold wash buffer (50 mM Tris, 150-300 mM NaCl). Elution buffers were made by adding 20-30 mM reduced L-Glutathione (Sigma-Aldrich, #G4251-25G) or 250 mM imidazole to elute GST- or MBP-tagged

proteins, respectively. For GST SPN, 1 mM DTT (Sigma-Aldrich, #D0632-5G) and 0.1 % triton-X were also added to the elution buffer. After addition of the eluting agent, the pH was adjusted to 7.0-8.0. Proteins were further dialyzed with Thermo Scientific Slide-A-Lyzer™ Dialysis Cassettes or subjected to gel filtration (described below). Eluted and dialyzed proteins were analyzed with SDS PAGE gel electrophoresis and Coomassie Blue staining (InstantBlue Protein Stain, expedeon, #ISB1L).

Gel filtration

The elution fraction from glutathione column was subjected to HiLoad 16/600 pg Superdex 200 gel filtration column (GE Healthcare, #-17-1069-01) preequilibrated with buffer containing 50 mM Hepes pH 8.0, 300 mM NaCl, 5 mM MgCl2, 5% glycerol, 0.02% sodium azide. The run was performed at 4°C with flow of 1 ml/min and fractions of 2 ml were collected. Proteins in fractions 17 were taken to co-sedimentation experiments fresh without any manipulations, after the protein concentrations were determined with Nanodrop using specific absorbance at 280 nm, calculated with Expasy ProtParam available online https://web.expasy.org/protparam/.

Co-sedimentation assays

Actin co-sedimentation assays were carried out essentially as described earlier [70]. Briefly, different amounts of β/γ-actin were polymerized for 30-40 minutes at RT in the presence of G-buffer (5 mM Tris-HCl pH 7.5, 0.2 mM DTT, 0.2 mM $CaCl_2$, 0.2 mM ATP) by addition of 5 mM $MgCl_2$, 1 mM EGTA, 0.2 mM ATP, 1 mM DTT and NaCl at a final concentration of 100 mM. 1 µM of GST- or MBP-tagged SPN/SPN-ARR WT or mutant variants in their respective buffers (for GST SPN 50 mM Tris-HCl pH 8.0, 150 mM NaCl, 1 mM DTT and 0.1 % triton-X; for GST-SPN-ARR proteins and MBP-SPN-ARR N52R – 50 mM HEPES pH 8.0, 300 mM NaCl, 5 mM $MgCl_2$, 5 % glycerol and 0.02 % Sodium Azide) were added to pre-polymerized actin samples and further incubated for 30 minutes. To sediment the polymerized actin filaments and bound proteins, the samples were subjected to either low (19000 rpm for GST SPN WT) or high speed (60000 rpm for GST SPN WT and SPN Q37A/R38A and at 50000 rpm for GST SPN-ARR WT, SPN-ARR-N52R and SPN-ARR Q37A/R38A/N52R, and MBP SPN-ARR N52R and MBP SPN-ARR Q37A/R38A/N52R) ultracentrifugation for 30 minutes at 20 ºC in a Beckman Optima MAX Ultracentrifuge using a TLA100 rotor. Equal proportions of supernatants and pellets were run on 4-20 % gradient, 10 or 12 % SDS-polyacrylamide gels (Mini-PROTEAN TGX

Precast Gels, Bio-Rad Laboratories Inc.), which were then stained with Coomassie Blue. The intensities of protein bands were quantified with ImageLab 6.0 program (Bio-Rad Laboratories Inc.), analyzed and plotted as actin-bound protein (µM, protein of interest in pellet) vs actin concentrations. Binding curves were fitted with 3 parameter exponential equation using SigmaPlot 11.0: $f = y_o + a * (1 - exp^{-b*x})$, where f is actin-bound protein in µM, y_o is the protein in the pellet in the absence of actin, a the maximum bound protein, x represents actin concentration in µM and b is the fitting parameter. Actin concentration when half of the protein is bound was estimated from the equation: $C_{\frac{1}{2}} = \frac{ln\ 0.5}{-b}$. Please note that a small fraction of SPN and SPN-ARR constructs used in this study pelleted on their own in high-speed co-sedimentation assay, but this does not affect interpretation of the data, because in these assays one measures the increase of protein in the pellet fraction in the presence of actin filaments.

To analyze the competition between actin and His-Rap1b (Cytoskeleton Inc, cat. no. RR02-A) binding to GST SPN or SPN-ARR N52R some modifications were made to the assay. First, His-Rap1b was converted to active form by loading with a 10-fold excess of GMPPCP (non-hydrolyzable analogue of GTP, #M3509-25MG, Sigma-Aldrich) for 20 h at +4 ºC in Exchange buffer (20 mM Tris-HCl pH 7.5, 150 mM NaCl, 10 mM $MgCl_2$, 1 mM DTT, 5 % sucrose and 1 % dextran). After incubation, the buffer was changed using Amicon buffer-exchange filters to either Buffer-1 (50 mM Tris-HCl pH 8.0, 300 mM NaCl, 5 mM $MgCl_2$, 5 % glycerol, 0.5 mM DTT and 0.1 % Triton-X) or Buffer-2 (50 mM HEPES pH 8.0, 300 mM NaCl, 5 mM $MgCl_2$, 5 % glycerol and 0.02 % Sodium Azide) for GST-SPN and GST-SPN-ARR N52, respectively. Co-sedimentation assays were always performed with freshly made active His-Rap1b. Two experimental setups were used. First, 12 µM of β/γ-actin was polymerized for 1 hour at RT, followed by incubation with active His-Rap1b (4 µM) and GST SPN (1 µM), added sequentially, for approx. 50 min at RT. Second, 2 µM of β/γ-actin was polymerized for about 30 – 40 min at RT, followed by incubation with GST-SPN-ARR N52R (1 µM) and different amounts of active His-Rap1b (0, 0.5, 1, 2, 4, 6 and 8 µM), added sequentially, for approx. 30 min at RT. The final NaCl concentration in samples was always maintained at 100 mM. Then samples containing different combinations of actin, His-Rap1b, GST-SPN or GST-SPN-ARR N52R proteins were sedimented for 30 minutes at 20 ºC in a Beckman Optima MAX Ultracentrifuge at 60000 rpm in a TLA100 rotor. Equal proportions of carefully separated supernatants and pellets

were run on 10 or 12 % SDS-polyacrylamide gels, which were processed as described above. The intensity values for GST-SPN and His-Rap1b were corrected using values of similar-sized-bands from actin-alone and actin-SPN samples before further quantification, because of minor contaminants in the actin prep. Results from competition assay were presented either as bar graphs for actin-bound GST-SPN in the presence of His-Rap1b (5 repetitions), or plotted as actin-bound GST-SPN-ARR N52R *vs* His-Rap1b concentrations. Binding curves were obtained from 3 independent experiments and fitted using exponential decay equation: $f = y_o + a * exp^{-b*x}$, where *f* is GST-SPN-ARR N52R protein bound to actin in µM, y_o is the parameter, describing amount of protein remaining bound to actin when His-Rap1b concentration is tending to infinity, *a* is the maximum bound protein in the absence of His-Rap1b, *x* represents His-Rap1b concentration in µM and *b* is the fitting parameter (SigmaPlot 11.0).

β/γ-actin disassembly assay

The steady-state rate of β/γ-actin filament disassembly was measured using a modified protocol described for muscle actin[70]. Samples of polymerized pyrene actin (4 µM) were mixed and incubated for 5 minutes with 1 or 2 µM GST SPN and 0.8 µM cofilin-1 both diluted with G-buffer (5 mM Hepes pH8, 0.2 mM $CaCl_2$, 0.2 mM ATP, 1 mM DTT), in the presence 0.8 µM cofilin-1 and in the absence of both. All protein mixtures were assembled in 1.5 ml Eppendorf tubes. The reaction was initiated by the addition of 6 µM vitamin D binding protein [DBP] (Human DBP, G8764, Sigma) directly in the fluorometric cuvettes. During the experiments, buffer conditions were constant: 20 mM HEPES pH 8, 100 mM KCl, 1 mM EGTA, 0.2 mM ATP. All measurements were carried out using the Agilent Cary Eclipse Fluorescence Spectrophotometer with BioMelt Bundle System (Agilent Technologies) with excitation at 365 nm (Ex. Slit = 5 nm) and emission at 407 nm (Em. Slit = 10 nm). Each measurement was carried out in triplicate.

Co-immunoprecipitation

GFP-Trap® agarose, RFP-Trap® agarose and RFP-Trap® magnetic agarose (ChromoTek, #GTA-100, RTA-100 and RTMA-100) were used to pull down GFP- and RFP-tagged proteins from cell lysate. HEK293 and U2OS cells were transfected as described earlier, lysed in IP lysis buffer (40 mM HEPES-NaOH, 75 mM NaCl, 2 mM EDTA, 1% NP-40 and protease and phosphatase inhibitor tablets). Lysates

were cleared by centrifugation and incubated with 30 µl of beads for 1 h at 4°C with rotation. The co-immunoprecipitated complexes were washed three times with the GFP IP wash buffer, resuspended in denaturating and reducing 4X Laemmli sample buffer and heated for 5 min at 95°C. GST-tagged recombinant proteins were bound to GSH sepharose and Macherey-Nagel Ni-Ted resin as described earlier and pull down assays were performed similarly to other co-immunoprecipitations, except for the IP wash buffer recipe which consisted of 20 mM Tris-Hcl (pH 7.5), 150 mM NaCl and 1 % NP-40. Samples were analyzed by SDS-PAGE followed by western blot.

Western Blot and Coomassie Blue staining

Purified recombinant proteins and protein extracts prepared from harvested cells or immunoprecipitation experiments in reducing Laemmli Sample Buffer were run on 4–20 % Mini-PROTEAN® TGX™ Precast Protein Gels of different comb and well-sizes (Bio-Rad, #456-1093, #456-1094, #456-1095, #456-1095). For western blotting, gels were transferred to 0.2 µm nitrocellulose Trans-Blot Turbo Transfer Pack, mini or midi format (Bio-Rad, #170-4158, #170-4159). After transfer, membranes were blocked in 1:1 PBS and Thermo Scientific™ Pierce™ StartingBlock™ (ThermoFisher Scientific, #10108313). Primary antibodies were incubated overnight at +4 ^{o}C, and secondary antibodies for 1 h at RT, both in rotation or shaking. All antibody dilutions were done in the blocking buffer. Membranes were washed between antibody additions and before detection with Tris-buffered saline with Tween® 20 (TBST) and stored in PBS. Alternatively, samples were run on self-cast 10 % gels, blotted on nitrocellulose membranes using Wet Blot, blocked with and stained in 5 % milk in TBST and detected using WesternBright ECL Western Blotting detection kit (#K-12045-D20, Advansta). For Coomassie Blue staining, the gels were stained with Instant Blue (Biotop, #ISB1L) according to the manufacturer's instructions. The Odyssey (LI-COR) infrared scanner and Bio-Rad Chemidoc were used to image membranes and gels.

Protein structure visualization and structure-based superimpositions

Pymol (The PyMOL Molecular Graphics System, Version 2.0 Schrödinger, LLC) together with the protein structure database (rcsb.org) were used to visualized different protein domains. Sequence alignment followed by structural superposition was carried out by using Pymol's align-function. In cases

of low sequence homology, Pymol's cealign function was used instead. Pymol was used under professional license for academics.

Multiple sequence alignment

MUSCLE multiple sequence alignment algorithm inside Geneious R8 (https://www.geneious.com) was used to align multiple protein sequences. Altogether, the Geneious software platform was used for all sequence-handling tasks in this study.

Simulation systems

SHANK3 SPN-ARR. System S1 is an atomistic model of the WT SPN-ARR domain (residues 2–347) of SHANK3. The model is based on the X-ray structure of the N-terminal domains of SHANK3 (PDB:5G4X)[29]. System S2 comprises a similar model where the residue N52 of the 5G4X structure is mutated to arginine. To complement this, in System S3 we constructed the N52R mutant from the coordinates of the X-ray structure of SHANK3–Rap1A (PDB:6KYK)[45], but without Rap1A proteins. Together these systems served to study the structural dynamics of the SPN-ARR domain in a water environment.

SHANK3 SPN-ARR with Rap1A. System S4 entails a SHANK3 SPN-ARR domain (residues 5–363) complexed with two GNP-loaded Rap1A proteins (residues 1–166). The complex was extracted from the SHANK3–Rap1A structure (PDB:6KYK)[45]. To expedite conformational sampling, SHANK3 was mutated to the N52R form, which in simulations of System 2 was observed to undergo structural opening. The Rap1A-bound SPN-ARR constructs in System S4 were compared to Systems S1-3 to shed light on the role of Rap1A in the dynamics of the SHANK3 N-terminal domains.

Free energy of opening in SHANK3 SPN-ARR. In Systems S5 and S6, we elucidated the free energy of SPN-ARR opening in the WT and N52R mutant systems, respectively. To this end, we used a series of umbrella sampling simulations where we sampled the opening of the SPN-ARR structure, using the distance between these two domains as the reaction coordinate. The simulation parameters of the systems (S1-S6) are described below.

Table: Description of simulated systems.

System	Protein components (mutation, residue range)	No. of water molecules (K^+, Cl^-)	No. of replicas x duration (ns)	PDB id.
S1	SHANK3 SPN-ARR (WT, 2–347)	59354 (171, 169)	4 x 2000	5G4X
S2	SHANK3 SPN-ARR (N52R, 2–347)	59386 (170, 169)	4 x 2000	5G4X
S3	SHANK3 SPN-ARR (N52R, 5–363)	59330 (169, 173)	4 x 2000	6KYK
S4	SHANK3 SPN-ARR (N52R, 5–363), 2 x Rap1A (WT, 1–166), 2x GNP	65065 (193,185)	8 x 2000	6KYK
S5	SHANK3 SPN-ARR (WT, 2–347)	61674 (170, 168)	7 x 300	5G4X
S6	SHANK3 SPN-ARR (N52R, 2–347)	61672 (169, 168)	7 x 300	5G4X

Simulation models

Simulation models were built using the CHARMM-GUI portal[66,67]. Accordingly, all the mutations and post-translational modifications were implemented with CHARMM-GUI[66]. Interactions were described by the all-atom CHARMM36m force field[68]. Water molecules were described by the TIP3P water model[71]. Potassium and chloride ions described by the CHARMM36m force field were added to neutralize the charge of the systems and to reach the physiological saline concentration (150 mM).

Simulation parameters

We used the GROMACS simulation software package (version 2018) to run the simulations[69]. Initiation of the simulation runs followed the general CHARMM-GUI protocol: the simulation systems were first energy-minimized and then equilibrated with position restraints acting on the solute atoms[68]. Key parameters of production simulations are described in Table 1. We used the leap-frog integrator with a timestep of 2 fs to propagate the simulations[72]. Periodic boundary conditions were applied in all three dimensions. Atomic neighbors were tracked using the Verlet lists, and bonds were constrained by the LINCS algorithm [73]. Lennard-Jones interactions were cut off at 1.2 nm, while electrostatic interactions were calculated using the smooth particle-mesh Ewald (PME) algorithm. The pressure of the system

was set to 1 bar and coupled isotropically using the Parrinello-Rahman barostat with a time constant of 5 ps[74]. Temperature was set to 310 K and coupled separately for solute and solvent atoms using the Nosé—Hoover thermostat with a time constraint of 1 ps. Simulation trajectories were saved every 100 ps. Random initial velocities were assigned for the atoms from the Boltzmann distribution at the beginning of each simulation. For the remaining parameters, we refer to the GROMACS 2018.8 defaults[69].

In the umbrella sampling simulations (systems S5 and S6), we opened the initially closed SPN-ARR structure by pulling the SPN domain away from the ARR domain using a series of umbrella sampling windows (see Table). Starting from the closed structure, we increased the SPN-ARR distance by 1.4 Å at a time between consecutive sampling windows. This ensured sufficient overlap between the consecutive windows. Here, we exploited the *pull_init* option of GROMACS to set a new distance for each of the 300 ns windows. All 300 ns per window were used for the analysis of the potential of mean force using the weighted histogram analysis method (WHAM), which is implemented as the *gmx wham* code in GROMACS[75]. In the sampling windows, a force constant of 1000 kJ mol^{-1} nm^{-2} was used to constrain the SPN domain at each distance from the ARR domain. Meanwhile, the ARR domain was restrained (1000 kJ mol^{-1} nm^{-2}) from the heavy atoms of residues 115-137, 154-170, 188-203, 221-237, 255-270, 288-303, and 321-333. These residues were selected because they span the entire length of the ARR domain but do not reside at its SPN binding interface. Error estimates were calculated by bootstrap analysis implemented within the *gmx wham* code.

Flow cytometry (FACS) analysis of β1-integrin activity

Cell-surface β1-integrin activity was analyzed in transfected CHO cells with a previously described, FACS-based assay[76]. CHO cells were detached using Hyclone® HyQTase (Thermo Fisher Scientific Inc, #SV300.30.01), and resuspended in warm, serum-free medium. The cells were incubated for 40 minutes in rotation at RT with Alexa Fluor 647-labelled fibronectin 7-10 fragment in the presence or absence of 5 mM EDTA (the negative control). The cells were washed with cold Tyrodes buffer (10 mM Hepes-NaOH pH 7.5, 137 mM NaCl, 2.68 mM KCl, 0.42 mM NaH_2PO_4, 1.7 mM $MgCl_2$, 11.9 mM $NaHCO_3$, 5 mM glucose, 0.1 % BSA) and were fixed with 2 % PFA in PBS for 10 min at RT. The PFA was washed away with cold tyrodes and cells were incubated with an anti-α5-integrin antibody (clone

PB1, Developmental Studies Hybridoma Bank) in Tyrodes for 30 min at RT with rotation followed by Alexa Fluor 555-conjugated secondary antibody in rotation for 30 min at RT. Cells were washed twice with Tyrodes and resuspended in PBS. The fluorescence signal was analyzed using LSRFortessa (BD Biosciences, Franklin Lakes, NJ) and analyzed using Flowing Software 2.5.1. Viable single cells were gated based on forward scatter area (FSC-A) and side scatter area (SSC-A). GFP-positive cells were further gated from the total population, and Alexa 647 intensity was measured for each sample. The results were normalized to total α5β1-integrin staining. The α5β1 integrin activation index was defined as AI = $(F–F_0)/(F_{integrin})$, where F is the geometric mean fluorescence intensity of fibronectin 7-10 binding and F_0 is the mean fluorescent intensity of fibronectin 7-10 binding in EDTA-containing negative control. $F_{integrin}$ is the normalized average mean fluorescence intensity of total α5β1 integrin (PB1).

Zebrafish microinjections, plasmids & *in vitro* transcription

To generate templates for mRNA *in vitro* transcription, GFP SHANK3 plasmids were digested with EcoRI and NotI and the plasmid backbone was isolated on agarose gel. Insert was annealed by using annealing oligonucleotides (-5´-*AATTCGATCGTAATACGACTCACTATAGGGA*-3´) and (5´-*GGCCTCCCTATAGTGAGTCGTATTACGATCG*-3´). Annealed product was ligated into digested vector using T4 DNA ligase (NEB). The ligated plasmid was transformed into DH5α competent bacteria. Plasmids were isolated from bacteria clones with NucleoSpin Plasmid Easypure kit (Macherey-Nagel) and screened using digestion with PvuI enzyme. Correct plasmids were linearized with PvuI and used in HiScribe™ T7 ARCA mRNA Kit (with tailing) (NEB) and purified with RNA-25 Clean & Concentrator RNA purification kit (Zymo Research).

Right after spawning, the embryos were collected and injected with 3.5 ng of either control morpholino oligo or with *shank3a (*AGAAAGTCTTGCGCTCTCACCTGGA) and/or *shank3b (*AGAAGCATCTCTCGTCACCTGAGGT) targeting morpholino oligos[53] into 1-4 cell stage embryos using Nanoject II microinjector (Drummond Scientific). To study the effects of shank3 mutations, *in vitro* transcribed mRNAs were co-injected into embryos. After injections, the embryos were placed in E3 medium (5 mM NaCl, 0.17 mM KCl, 0.33 mM $CaCl_2$, 0.33 mM $MgSO_4$) supplemented with pen/strep and incubated at 28.5°C.

Zebrafish motility assay

To analyse motility of zebrafish embryos, 15 µl of 2mg/ml pronase solution was added a day after injections to facilitate hatching. At two days post fertilization, the embryos were transferred to 96-well plates (1 embryo/well). The motility analysis was carried out at 28.5°C using Daniovision instrument (Noldus IT) by imaging the plate at 30 fps for 60 min. First, a 30 min baseline was followed by three 10 min cycles of light/dark (5 min each). After this, 20 mM pentylenetetrazole (PTZ, Sigma-Aldrich) was added to stimulate motility of embryos and a similar program was run again. The speed and total distance moved was analysed using Ethovison XT software (Noldus IT). The first 20 min of baseline was removed and remaining 40 min was used in statistical analyses. Movements were filtered using 0.2 mm minimum distance filter, to reduce background noise, and a maximum movement filter of 4 mm. Average swim speed, total distance moved and the fraction of time spent moving were quantified.

Zebrafish eye pigmentation assay

To analyse the effects on zebrafish eye pigmentation, the microinjected embryos of 30 hpf (hours post fertilization) of age were dechorionated using forceps. After dechorionation, embryos were anesthetized using Tricaine (160 mg/ml) and imaged using Zeiss AxioZOOM stereomicroscope. Image analysis was carried out using ImageJ/FIJI. First, the images were inverted and background was removed (radius 50). Then, the eyes were outlined manually with a segmented line selection tool and intensity was measured.

Quantification and Statistical Analysis

Unless otherwise indicated, all quantified experiments were replicated at least three times. No strategy was employed for randomization and/or stratification. No blinding or sample-size estimations were performed at any stage of the study. No data were excluded from the analyses. Whenever data were deemed to follow a non-normal distribution (according to Shapiro-Wilk normality test), analyses were conducted using non-parametric methods. The names and/or numbers of individual statistical tests, samples and data points are indicated in figure legends. All statistical analyses were performed with GraphPad Prism 7 or 8 software and a P-value 0.05 or less was considered as statistically significant.

KEY RESOURCES TABLE

REAGENT or RESOURCE	SOURCE	IDENTIFIER
Antibodies		
Mouse monoclonal anti-β-actin (clone AC-15) – dilution 1:1000 for WB	Sigma-Aldrich	Cat no. A1978
Mouse monoclonal anti-GFP (clone 9F9.F9) – dilution 1:1000 for WB	Abcam	Cat no. ab1218
Mouse monoclonal anti-GFP – dilution 1:3000 for WB	Covance	Cat no. MMS-118P-500
Mouse monoclonal anti-vinculin (clone hVIN-1) - dilution 1:500 for IF	Sigma-Aldrich	Cat no. V9131
Mouse active β1 integrin (12G10) – dilution 1:100 for IF	In-house, hybridoma	N/A
Hamster integrin α5 (clone PB12) – dilution 1:10 for FACS	Developmental Studies Hybridoma Bank	N/A
Rabbit anti-GFP – dilution 1:1000 for WB	Abcam	Cat no. ab69507
Rabbit anti-GST – dilution 1:1000 for WB	Cell Signalling Technology	Cat no. 91G1
Rabbit anti-non-muscle myosin heavy chain II (clone Poly19098) – dilution 1:1000 for IF	BioLegend	Cat no. 909801
Rabbit anti-RFP – dilution 1:1000 for WB	Invitrogen	R10367
Rabbit anti-RFP – dilution 1:1000 for WB	Chromotek	Cat no. 5F8
Rabbit anti-vesicular glutamate transporter (vGlut1) – dilution 1:2000 for IF	Synaptic Systems	Cat no. 135 303
Anti-mouse or anti-rabbit Alexa Fluor 488-, 555- and 568-conjugated secondary antibodies – dilutions 1:300 for IF	Invitrogen/Life Technologies	Cat no. A-21202; A-21424; A10037; A31571; A-31573
Anti-mouse or anti-rabbit IrDye 680 and IrDye 800 – dilution 1:5000 for WB	LI-COR	Cat no. 926-68072; 926-32212; 926-68073; 926-32213
Bacterial and Virus Strains		
Competent E. coli BL21 bacteria	Merck	Cat. no. 70954
Competent E. coli DH5α bacteria	ThermoFisher Scientific	Cat. no. 18265017
Chemicals, Peptides, and Recombinant Proteins		
Atto-Phalloidin-647 – dilution 1:500 for IF	Sigma	Cat. no. 65906
Atto-Phalloidin-740 – dilution 1:75 for IF	Sigma	Cat. no. 07373
Phalloidin Alexa Fluor 488 or 647 – dilution 1:200 for IF	Invitrogen	Cat. no. A12379; A22287
SiR-actin-647 – dilution 1:5000 for IF	Spirochrome	Cat. no. SC001
Bovine plasma fibronectin	Merck-Millipore	Cat. no. 341631
Fibronectin 7-10 fragment	Produced in house	N/A
Lipofectamine™ 2000 Transfection Reagent	Thermo Fisher Scientific Inc	Cat. no. 11668019
Lipofectamine 3000 and P3000™ Enhancer Reagent	Thermo Fisher Scientific Inc	Cat. no. L3000-015

GMPPCP	Sigma-Aldrich	Cat. no. M3509-25MG
Pentylenetetrazole	Sigma-Aldrich	Cat. no. P6500
cOmplete™ protease inhibitor	Roche	Cat. no. #5056489001
GST-SPN-WT	This study	N/A
GST-SPN-Q37A/R38A	This study	N/A
GST-SPN-ARR-WT	This study	N/A
GST-SPN-ARR-N52R	This Study	N/A
GST-SPN-ARR-Q37A/R37A/N52R	This study	N/A
His-MBP-SPN-ARR-N52R	This Study	N/A
His-MBP-SPN-ARR-Q37A/R37A/N52R	This study	N/A
His-Rap1b	Cytoskeleton Inc	Cat. no. RR02-A
Human vitamin D binding protein	Sigma-Aldrich	Cat. no. G8764
Critical Commercial Assays		
N/A		
Deposited Data		
N/A		
Experimental Models: Cell Lines		
CHO (Chinese hamster ovary) cells	[61]	N/A
HEK293 (human embryonic kidney) cells	ATCC	Cat. no. CRL-1573
U2OS osteosarcoma cells	Leibniz Institute DSMZ-German Collection of Microorganisms and Cell Cultures, Braunschweig DE	Cat. no. ACC 785
Experimental Models: Organisms/Strains		
Wild-type (AB strain) zebrafish embryos	Tampere Zebrafish Laboratory (Tampere, Finland)	N/A
Oligonucleotides		
Morpholino - *shank3a* AGAAAGTCTTGCGCTCTCACCTGGA	Gene Tools LLC (Philomath (OR), USA)	N/A
Morpholino - *shank3b* AGAAGCATCTCTCGTCACCTGAGGT	Gene Tools LLC (Philomath (OR), USA)	N/A
Recombinant DNA		
GFP-SHANK3-WT	Alex Shcheglovitov (Univ. of Utah, Salt Lake City); [29,62]	N/A
GFP-SHANK3-Q37A/R38A	This study	N/A
GFP-SHANK3-Q37A/R38A/N52R	This study	N/A
GFP-SHANK3-N52R	This study	N/A
GFP-SHANK3-SPN (GFP-SPN-WT)	[29,44]	N/A
GFP-SPN-Q37A/R38A	This study	N/A
GFP-SPN-R12C	[29]	N/A
GFP-SHANK3-SPN-ARR (GFP-SPN-ARR-WT)	This study	N/A
GFP-SPN-ARR-Q37A/R38A/N52R	This study	N/A
GFP-SPN-ARR-N52R	This study	N/A
SHANK3 1-1731-mRFP (full-length)	[44]	N/A

SHANK3 1-339-mRFP (SPN-ARR-WT-mRFP)	[44]	N/A
SPN-ARR-N52R-mRFP	This study	N/A
SHANK3 1-376-mRFP	[37]	N/A
SHANK3 1-538-mRFP	[44]	N/A
SHANK3 1-676-mRFP	[37]	N/A
SHANK3 1-835-mRFP	[37]	N/A
SHANK3 1-1334-mRFP	This study	N/A
pEGFP-C3-Rap1Q63E	Buzz Baum (MRC-LMCB, London, UK) and Stephen Royle (University of Warwick, UK); [63,64]	N/A
MYO10-mCherry	Addgene (Staffan Strömblad)	Cat. no. 139780
kindlin-2-GFP	Maddy Parsons (King's College London, UK)	N/A
GFP-talin-1	Ben Goult (University of Kent, UK)	N/A
mRuby-Lifeact	Addgene	Cat. no. 54560
mRFP-N1	Addgene	Cat. no. 54635
pEGFP-C1	BD Biosciences/Clontech	N/A - discontinued
tD-tomato-N1	Clontech	N/A - discontinued
pCoofy4	Addgene	Cat. no. 43986
Software and Algorithms		
Flowing Software 2.5.1	Cell Imaging & cytometry Core facility, Turku Bioscience Centre	http://flowingsoftware.btk.fi/
GraphPad Prism 7.01	Graphpad Software	http:// https://www.graphpad.com/
Fiji	NIH, open source; [65]	https://fiji.sc/
Neurolucida Explorer	MBF Bioscience	https://www.mbfbioscience.com/neurolucida-explorer
Pymol (The PyMOL Molecular Graphics System, Version 2.0)	Schrödinger, LLC	https://pymol.org/2/
MUSCLE multiple sequence alignment algorithm	Geneious R8	https://www.geneious.com
CHARMM-GUI	[66–68]	http://www.charmm-gui.org/
GROMACS simulation software package (version 2018)	[69]	https://www.gromacs.org/
Ethovison XT software	Noldus IT	https://www.noldus.com/ethovision-xt
SigmaPlot 11.0	Systat Software Inc	http://www.sigmaplot.co.uk/
ProtParam	Expasy	https://web.expasy.org/protparam/
Other		
BugBuster	Merck Millipore	Cat. no. 70584-4

DNAse I	Sigma-Aldrich	Cat. no. 11284932001
Glutathione Sepharose® 4B	GE Healthcare	Cat. no. 17-0756-01
Protino Ni-TED resin	Macherey-Nagel	Cat. no. 745200.5
HiScribe™ T7 ARCA mRNA kit (with tailing)	New England Biolabs	Cat. no. E2060S
NEBuilder cloning kit	New England Biolabs	Cat. no. E5520S
QuikChange II XL site-directed mutagenesis kit	Agilent	Cat. no. 200521
RNA-25 Clean & Concentrator RNA purification kit	Zymo Research	Cat. no. R1017
GFP-Trap® agarose, RFP-Trap® agarose and RFP-Trap® magnetic agarose	ChromoTek	Cat. no.; GTA-100, RTA-100, RTMA-100

Supplemental Video Legends

Supplementary Video 1. Atomistic MD simulation of SHANK3 SPN-ARR as both the wild-type and N52R mutant (Systems S1 and S2 in Table 1). The ARR domains are colored orange while the SPN domains are depicted in cyan. Amino acid residues of the ARR domain that are within 0.3 nm from residue 52 are highlighted with licorice representation.

Supplementary Video 2. Atomistic MD simulation of the N52R mutant of SHANK3 SPN-ARR bound to two Rap1 proteins (System S4 in Table 1). The ARR domains are colored orange while the SPN domains are depicted in cyan. Rap1 molecules are colored with shades of green. Residues R52 and R179 are highlighted with blue beads.

References

1. Jacquemet, G., Hamidi, H., and Ivaska, J. (2015). Filopodia in cell adhesion, 3D migration and cancer cell invasion. Curr Opin Cell Biol *36*, 23–31.

2. Joensuu, M., Lanoue, V., and Hotulainen, P. (2018). Dendritic spine actin cytoskeleton in autism spectrum disorder. Prog Neuropsychopharmacol Biol Psychiatry *8*;84(Pt B):362-381.

3. Clayton, N.S., and Ridley, A.J. (2020). Targeting Rho GTPase Signaling Networks in Cancer. Front Cell Dev Biol *8*, 222.

4. Warner, H., Wilson, B.J., and Caswell, P.T. (2019). Control of adhesion and protrusion in cell migration by Rho GTPases. Curr Opin Cell Biol *56*, 64–70.

5. Papalazarou, V., and Machesky, L.M. (2020). The cell pushes back: The Arp2/3 complex is a key orchestrator of cellular responses to environmental forces. Curr Opin Cell Biol *68*, 37–44.

6. Leblond, C.S., Nava, C., Polge, A., Gauthier, J., Huguet, G., Lumbroso, S., Giuliano, F., Stordeur, C., Depienne, C., Mouzat, K., et al. (2014). Meta-analysis of SHANK Mutations in Autism Spectrum Disorders: A Gradient of Severity in Cognitive Impairments. PLoS Genetics *10*(9): e1004580.

7. Moessner, R., Marshall, C.R., Sutcliffe, J.S., Skaug, J., Pinto, D., Vincent, J., Zwaigenbaum, L., Fernandez, B., Roberts, W., Szatmari, P., et al. (2007). Contribution of SHANK3 Mutations to Autism Spectrum Disorder. The American Journal of Human Genetics *81*(6):1289-97.

8. Durand, C.M., Betancur, C., Boeckers, T.M., Bockmann, J., Chaste, P., Fauchereau, F., Nygren, G., Rastam, M., Gillberg, I.C., Anckarsäter, H., et al. (2007). Mutations in the gene encoding the synaptic scaffolding protein SHANK3 are associated with autism spectrum disorders. Nature Genetics *39*(1):25-7.

9. Satterstrom, F.K., Kosmicki, J.A., Wang, J., Breen, M.S., De Rubeis, S., An, J.-Y., Peng, M., Collins, R., Grove, J., Klei, L., et al. (2020). Large-Scale Exome Sequencing Study Implicates Both Developmental and Functional Changes in the Neurobiology of Autism. Cell *180*, 568-584.e23.

10. Zhu, L., Wang, X., Li, X.-L., Towers, A., Cao, X., Wang, P., Bowman, R., Yang, H., Goldstein, J., Li, Y.-J., et al. (2014). Epigenetic dysregulation of SHANK3 in brain tissues from individuals with autism spectrum disorders. Hum. Mol. Genet. *23*, 1563–1578.

11. Gauthier, J., Champagne, N., Lafrenière, R.G., Xiong, L., Spiegelman, D., Brustein, E., Lapointe, M., Peng, H., Côté, M., Noreau, A., et al. (2010). De novo mutations in the gene encoding the synaptic scaffolding protein SHANK3 in patients ascertained for schizophrenia. Proc Natl Acad Sci U S A *27*;107(17):7863-8.

12. Phelan, K., and McDermid, H.E. (2012). The 22q13.3 deletion syndrome (Phelan-McDermid syndrome). Mol Syndromol *2*(3-5):186-201.

13. Sarasua, S.M., Boccuto, L., Sharp, J.L., Dwivedi, A., Chen, C.F., Rollins, J.D., Rogers, R.C., Phelan, K., and DuPont, B.R. (2014). Clinical and genomic evaluation of 201 patients with Phelan-McDermid syndrome. Hum Genet *133*(7):847-59.

14. Kathuria, A., Nowosiad, P., Jagasia, R., Aigner, S., Taylor, R.D., Andreae, L.C., Gatford, N.J.F., Lucchesi, W., Srivastava, D.P., and Price, J. (2018). Stem cell-derived neurons from autistic individuals with SHANK3 mutation show morphogenetic abnormalities during early development. Mol Psychiatry *23*, 735–746.

15. Sarowar, T., and Grabrucker, A.M. (2016). Actin-Dependent Alterations of Dendritic Spine Morphology in Shankopathies. Neural Plast *2016*:8051861.

16. Duffney, L.J., Zhong, P., Wei, J., Matas, E., Cheng, J., Qin, L., Ma, K., Dietz, D.M., Kajiwara, Y., Buxbaum, J.D., et al. (2015). Autism-like Deficits in Shank3-Deficient Mice Are Rescued by Targeting Actin Regulators. Cell Rep *11*, 1400–1413.

17. Wang, L., Pang, K., Han, K., Adamski, C.J., Wang, W., He, L., Lai, J.K., Bondar, V.V., Duman, J.G., Richman, R., et al. (2020). An autism-linked missense mutation in SHANK3 reveals the modularity of Shank3 function. Mol Psychiatry, *25*(10):2534-2555.

18. Qualmann, B. (2004). Linkage of the Actin Cytoskeleton to the Postsynaptic Density via Direct Interactions of Abp1 with the ProSAP/Shank Family. J Neurosci *24*(10):2481-95.

19. Haeckel, A., Ahuja, R., Gundelfinger, E.D., Qualmann, B., and Kessels, M.M. (2008). The Actin-Binding Protein Abp1 Controls Dendritic Spine Morphology and Is Important for Spine Head and Synapse Formation. J Neurosci *28*(40): 10031–10044.

20. Böckers, T.M., Mameza, M.G., Kreutz, M.R., Bockmann, J., Weise, C., Buck, F., Richter, D., Gundelfinger, E.D., and Kreienkamp, H.J. (2001). Synaptic scaffolding proteins in rat brain: Ankyrin repeats of the multidomain Shank protein family interact with the cytoskeletal protein α-fodrin. J Biol Chem *276*(43):40104-12.

21. Khan, M.H., Salomaa, S.I., Jacquemet, G., Butt, U., Miihkinen, M., Deguchi, T., Kremneva, E., Lappalainen, P., Humphries, M.J., and Pouwels, J. (2017). The Sharpin interactome reveals a role for Sharpin in lamellipodium formation via the Arp2/3 complex. J Cell Sci *130*(18):3094-3107.

22. Park, E., Na, M., Choi, J., Kim, S., Lee, J.R., Yoon, J., Park, D., Sheng, M., and Kim, E. (2003). The Shank family of postsynaptic density proteins interacts with and promotes synaptic accumulation of the βPIX guanine nucleotide exchange factor for Rac1 and Cdc42. J Biol Chem *278*(21):19220-9.

23. Stephenson, J.R., Wang, X., Perfitt, T.L., Parrish, W.P., Shonesy, B.C., Marks, C.R., Mortlock, D.P., Nakagawa, T., Sutcliffe, J.S., and Colbran, R.J. (2017). A Novel Human CAMK2A Mutation Disrupts Dendritic Morphology and Synaptic Transmission, and Causes ASD-Related Behaviors. J Neurosci *37*, 2216–2233.

24. Jeong, J., Li, Y., and Roche, K.W. (2021). CaMKII Phosphorylation Regulates Synaptic Enrichment of Shank3. eNeuro *8(3)*, ENEURO.0481-20.2021.

25. Bockmann, J., Kreutz, M.R., Gundelfinger, E.D., and Böckers, T.M. (2002). ProSAP/Shank postsynaptic density proteins interact with insulin receptor tyrosine kinase substrate IRSp53. J Neurochem *83*(4):1013-7.

26. Naisbitt, S., Eunjoon, K., Tu, J.C., Xiao, B., Sala, C., Valtschanoff, J., Weinberg, R.J., Worley, P.F., and Sheng, M. (1999). Shank, a novel family of postsynaptic density proteins that binds to the NMDA receptor/PSD-95/GKAP complex and cortactin. Neuron *23*, 569–582.

27. Du, Y., Weed, S.A., Xiong, W.C., Marshall, T.D., and Parsons, J.T. (1998). Identification of a novel cortactin SH3 domain-binding protein and its localization to growth cones of cultured neurons. Mol. Cell. Biol. *18*, 5838–5851.

28. Durand, C.M., Perroy, J., Loll, F., Perrais, D., Fagni, L., Bourgeron, T., Montcouquiol, M., and Sans, N. (2012). SHANK3 mutations identified in autism lead to modification of dendritic spine morphology via an actin-dependent mechanism. Molecular Psychiatry *17*, 71–84.

29. Lilja, J., Zacharchenko, T., Georgiadou, M., Jacquemet, G., Franceschi, N.D., Peuhu, E., Hamidi, H., Pouwels, J., Martens, V., Nia, F.H., et al. (2017). SHANK proteins limit integrin activation by directly interacting with Rap1 and R-Ras. Nature Cell Biology *19*, 292–305.

30. Pellinen, T., Rantala, J.K., Arjonen, A., Mpindi, J.P., Kallioniemi, O., and Ivaska, J. (2012). A functional genetic screen reveals new regulators of β1-integrin activity. J Cell Sci *125*(Pt 3):649-61.

31. Jacquemet, G., Baghirov, H., Georgiadou, M., Sihto, H., Peuhu, E., Cettour-Janet, P., He, T., Perälä, M., Kronqvist, P., Joensuu, H., et al. (2016). L-type calcium channels regulate filopodia stability and cancer cell invasion downstream of integrin signalling. Nat Commun *7*:13297.

32. Lagarrigue, F., Vikas Anekal, P., Lee, H.-S., Bachir, A.I., Ablack, J.N., Horwitz, A.F., and Ginsberg, M.H. (2015). A RIAM/lamellipodin–talin–integrin complex forms the tip of sticky fingers that guide cell migration. Nat Commun *6*:8492.

33. Jacquemet, G., Stubb, A., Saup, R., Miihkinen, M., Kremneva, E., Hamidi, H., and Ivaska, J. (2019). Filopodome Mapping Identifies p130Cas as a Mechanosensitive Regulator of Filopodia Stability. Curr Biol *29*(2): 202-216.e7.

34. Zhang, H., Berg, J.S., Li, Z., Wang, Y., Lång, P., Sousa, A.D., Bhaskar, A., Cheney, R.E., and Strömblad, S. (2004). Myosin-X provides a motor-based link between integrins and the cytoskeleton. Nat Cell Biol *6*, 523–531.

35. Cochoy, D.M., Kolevzon, A., Kajiwara, Y., Schoen, M., Pascual-Lucas, M., Lurie, S., Buxbaum, J.D., Boeckers, T.M., and Schmeisser, M.J. (2015). Phenotypic and functional analysis of SHANK3 stop mutations identified in individuals with ASD and/or ID. Mol Autism *6:*23.

36. Grabrucker, S., Proepper, C., Mangus, K., Eckert, M., Chhabra, R., Schmeisser, M.J., Boeckers, T.M., and Grabrucker, A.M. (2014). The PSD protein ProSAP2/Shank3 displays synapto-nuclear shuttling which is deregulated in a schizophrenia-associated mutation. J Exp Neurol *1253*:126-137.

37. Nia, F.H., Woike, D., Kloth, K., Kortüm, F., and Kreienkamp, H.-J. Truncating mutations in SHANK3 associated with global developmental delay interfere with nuclear β-catenin signaling. J Neurochem *155(3)*:250-263.

38. Goult, B.T., Bouaouina, M., Elliott, P.R., Bate, N., Patel, B., Gingras, A.R., Grossmann, J.G., Roberts, G.C.K., Calderwood, D.A., Critchley, D.R., et al. (2010). Structure of a double ubiquitin-like domain in the talin head: A role in integrin activation. EMBO J *29(6)*:1069-1080.

39. Bledzka, K., Bialkowska, K., Sossey-Alaoui, K., Vaynberg, J., Pluskota, E., Qin, J., and Plow, E.F. (2016). Kindlin-2 directly binds actin and regulates integrin outside-in signaling. J Cell Biol *213*(1):97-108.

40. Campellone, K.G., and Welch, M.D. (2010). A Nucleator Arms Race: Cellular Control of Actin Assembly. Nat Rev Mol Cell Biol *11*, 237–251.

41. Chesarone, M.A., DuPage, A.G., and Goode, B.L. (2010). Unleashing formins to remodel the actin and microtubule cytoskeletons. Nat Rev Mol Cell Biol *11*, 62–74.

42. Goult, B.T., Yan, J., and Schwartz, M.A. (2018). Talin as a mechanosensitive signaling hub. J Cell Biol *217*, 3776–3784.

43. Gary, R., and Bretscher, A. (1995). Ezrin self-association involves binding of an N-terminal domain to a normally masked C-terminal domain that includes the F-actin binding site. Mol. Biol. Cell *6*, 1061–1075.

44. Mameza, M.G., Dvoretskova, E., Bamann, M., Hönck, H.H., Güler, T., Boeckers, T.M., Schoen, M., Verpelli, C., Sala, C., Barsukov, I., et al. (2013). SHANK3 gene mutations associated with autism facilitate ligand binding to the shank3 ankyrin repeat region. J Biol Chem *288*(37):26697-708.

45. Cai, Q., Hosokawa, T., Zeng, M., Hayashi, Y., and Zhang, M. (2019). Shank3 Binds to and Stabilizes the Active Form of Rap1 and HRas GTPases via Its NTD-ANK Tandem with Distinct Mechanisms. Structure *3*:290-300.

46. Mei, Y., Monteiro, P., Zhou, Y., Kim, J.A., Gao, X., Fu, Z., and Feng, G. (2016). Adult restoration of Shank3 expression rescues selective autistic-like phenotypes. Nature *530*(7591):481-484.

47. Welie, I. van, and Spier, A.D. (2002). Actin dynamics in dendritic spines. Trends in Neurosciences *25*, 290.

48. Zeng, M., Chen, X., Guan, D., Xu, J., Wu, H., Tong, P., and Zhang, M. (2018). Reconstituted Postsynaptic Density as a Molecular Platform for Understanding Synapse Formation and Plasticity. Cell *174*, 1172-1187.e16.

49. Baron, M.K., Boeckers, T.M., Vaida, B., Faham, S., Gingery, M., Sawaya, M.R., Salyer, D., Gundelfinger, E.D., and Bowie, J.U. (2006). An architectural framework that may lie at the core of the postsynaptic density. Science 311(5760):531-5.

50. Schmeisser, M.J., Ey, E., Wegener, S., Bockmann, J., Stempel, A.V., Kuebler, A., Janssen, A.-L., Udvardi, P.T., Shiban, E., Spilker, C., et al. (2012). Autistic-like behaviours and hyperactivity in mice lacking ProSAP1/Shank2. Nature *486*, 256–260.

51. Wang, X., Xu, Q., Bey, A.L., Lee, Y., and Jiang, Y. (2014). Transcriptional and functional complexity of Shank3 provides a molecular framework to understand the phenotypic heterogeneity of SHANK3 causing autism and Shank3 mutant mice. Mol Autism *5*, 30.

52. Liu, C., Li, C., Hu, C., Wang, Y., Lin, J., Jiang, Y., Li, Q., and Xu, X. (2018). CRISPR/Cas9-induced shank3b mutant zebrafish display autism-like behaviors. Molecular Autism *9*, 23.

53. Kozol, R.A., Cukier, H.N., Zou, B., Mayo, V., De Rubeis, S., Cai, G., Griswold, A.J., Whitehead, P.L., Haines, J.L., Gilbert, J.R., et al. (2015). Two knockdown models of the autism genes SYNGAP1 and SHANK3 in zebrafish produce similar behavioral phenotypes associated with embryonic disruptions of brain morphogenesis. Hum Mol Genet *24*, 4006–4023.

54. Baraban, S.C., Taylor, M.R., Castro, P.A., and Baier, H. (2005). Pentylenetetrazole induced changes in zebrafish behavior, neural activity and c-fos expression. Neurosci *131*, 759–768.

55. Lee, H.-S., Lim, C.J., Puzon-McLaughlin, W., Shattil, S.J., and Ginsberg, M.H. (2009). RIAM Activates Integrins by Linking Talin to Ras GTPase Membrane-targeting Sequences. J Biol Chem *284*, 5119–5127.

56. Bromberger, T., Zhu, L., Klapproth, S., Qin, J., and Moser, M. (2019). Rap1 and membrane lipids cooperatively recruit talin to trigger integrin activation. J Cell Sci *132*.

57. Lawson, C.D., and Burridge, K. (2014). The on-off relationship of Rho and Rac during integrin-mediated adhesion and cell migration. Small GTPases *5*.

58. Huveneers, S., and Danen, E.H.J. (2009). Adhesion signaling – crosstalk between integrins, Src and Rho. J Cell Sci *122*, 1059–1069.

59. Sun, Z., Costell, M., and Fässler, R. (2019). Integrin activation by talin, kindlin and mechanical forces. Nat Cell Biol *21*, 25–31.

60. Kechagia, J.Z., Ivaska, J., and Roca-Cusachs, P. (2019). Integrins as biomechanical sensors of the microenvironment. Nat Rev Mol Cell Biol *20*, 457–473.

61. Esko, J.D., Stewart, T.E., and Taylor, W.H. (1985). Animal cell mutants defective in glycosaminoglycan biosynthesis. PNAS *82*, 3197–3201.

62. Shcheglovitov, A., Shcheglovitova, O., Yazawa, M., Portmann, T., Shu, R., Sebastiano, V., Krawisz, A., Froehlich, W., Bernstein, J.A., Hallmayer, J.F., et al. (2013). SHANK3 and IGF1 restore synaptic deficits in neurons from 22q13 deletion syndrome patients. Nature *503*, 267–271.

63. Kaur, S., Fielding, A.B., Gassner, G., Carter, N.J., and Royle, S.J. (2014). An unmet actin requirement explains the mitotic inhibition of clathrin-mediated endocytosis. eLife *3*, e00829.

64. Dao, V.T., Dupuy, A.G., Gavet, O., Caron, E., and de Gunzburg, J. (2009). Dynamic changes in Rap1 activity are required for cell retraction and spreading during mitosis. J. Cell. Sci. *122*, 2996–3004.

65. Schindelin, J., Arganda-Carreras, I., Frise, E., Kaynig, V., Longair, M., Pietzsch, T., Preibisch, S., Rueden, C., Saalfeld, S., Schmid, B., et al. (2012). Fiji: an open-source platform for biological-image analysis. Nat Methods *9*, 676–682.

66. Jo, S., Lim, J.B., Klauda, J.B., and Im, W. (2009). CHARMM-GUI Membrane Builder for Mixed Bilayers and Its Application to Yeast Membranes. Biophys J *97*, 50–58.

67. Wu, E.L., Cheng, X., Jo, S., Rui, H., Song, K.C., Dávila-Contreras, E.M., Qi, Y., Lee, J., Monje-Galvan, V., Venable, R.M., et al. (2014). CHARMM-GUI Membrane Builder Toward Realistic Biological Membrane Simulations. J Comput Chem *35*, 1997–2004.

68. Lee, J., Cheng, X., Swails, J.M., Yeom, M.S., Eastman, P.K., Lemkul, J.A., Wei, S., Buckner, J., Jeong, J.C., Qi, Y., et al. (2016). CHARMM-GUI Input Generator for NAMD, GROMACS, AMBER, OpenMM, and CHARMM/OpenMM Simulations Using the CHARMM36 Additive Force Field. J Chem Theory Comput *12*, 405–413.

69. Abraham, M.J., Murtola, T., Schulz, R., Páll, S., Smith, J.C., Hess, B., and Lindahl, E. (2015). GROMACS: High performance molecular simulations through multi-level parallelism from laptops to supercomputers. SoftwareX *1–2*, 19–25.

70. Kremneva, E., Makkonen, M.H., Skwarek-Maruszewska, A., Gateva, G., Michelot, A., Dominguez, R., and Lappalainen, P. (2014). Cofilin-2 controls actin filament length in muscle sarcomeres. Dev Cell *31*, 215–226.

71. Mark, P., and Nilsson, L. (2001). Structure and Dynamics of the TIP3P, SPC, and SPC/E Water Models at 298 K. J. Phys. Chem. A *105*, 9954–9960.

72. Gunsteren, W.F.V., and Berendsen, H.J.C. (1988). A Leap-frog Algorithm for Stochastic Dynamics. Molecular Simulation *1*, 173–185.

73. Hess, B., Bekker, H., Berendsen, H.J.C., and Fraaije, J.G.E.M. (1997). LINCS: A linear constraint solver for molecular simulations. J Comput Chem*18*, 1463–1472.

74. Parrinello, M., and Rahman, A. (1981). Polymorphic transitions in single crystals: A new molecular dynamics method. J Appl Phys *52*, 7182–7190.

75. Hub, J.S., de Groot, B.L., and van der Spoel, D. (2010). g_wham—A Free Weighted Histogram Analysis Implementation Including Robust Error and Autocorrelation Estimates. J. Chem. Theory Comput. *6*, 3713–3720.

76. Bouaouina, M., Harburger, D.S., and Calderwood, D.A. (2012). Talin and signaling through integrins. Methods Mol Biol *757*, 325–347.

1143

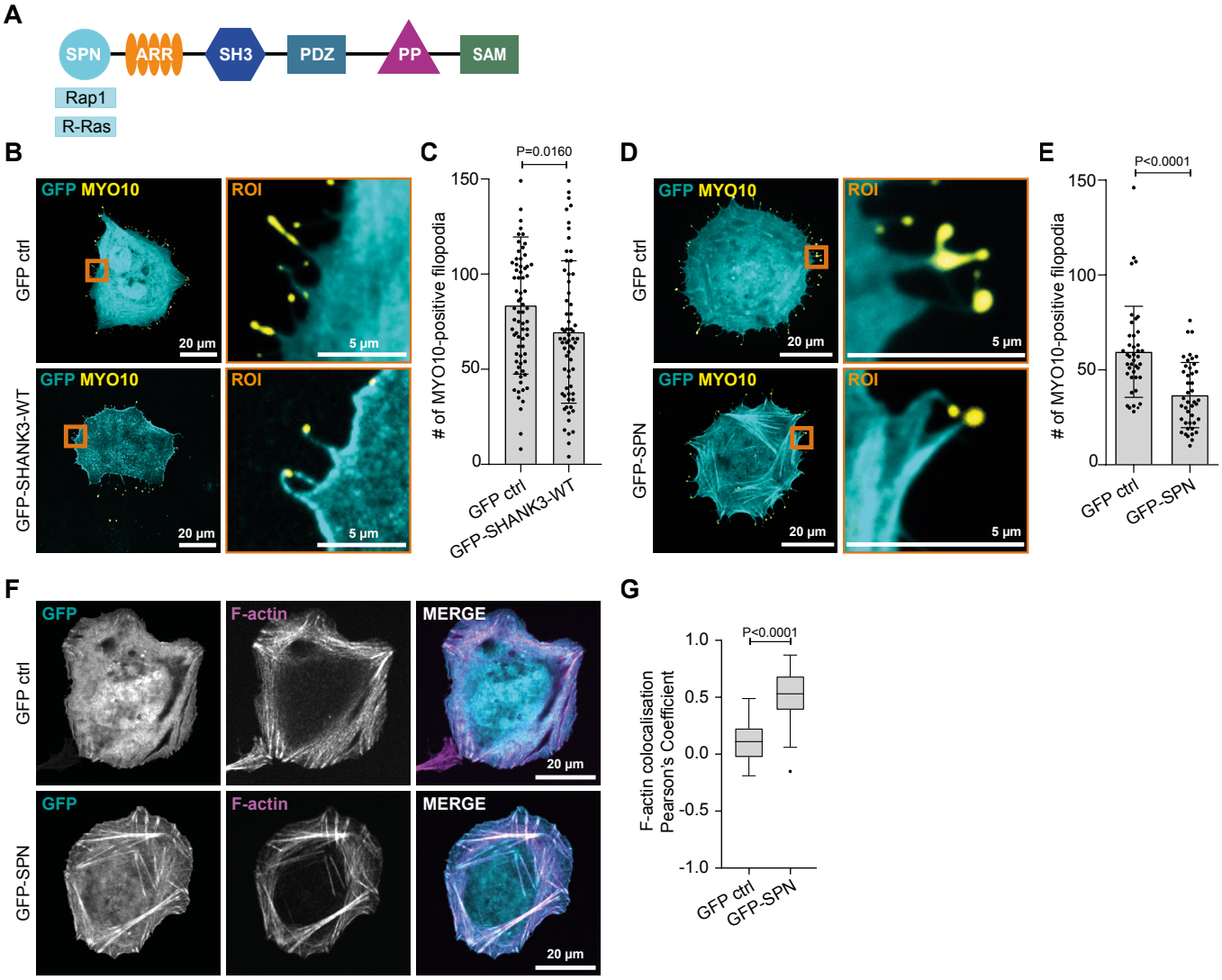
A
SPN
ARR
SH3
PDZ
PP
SAM
Rap1
R-Ras
B
GFP MYO10
ROI
GFP ctrl
GFP-SHANK3-WT
20 µm
5 µm
C
P=0.0160
# of MYO10-positive filopodia
150
100
50
0
GFP ctrl
GFP-SHANK3-WT
D
GFP MYO10
ROI
GFP ctrl
GFP-SPN
20 µm
5 µm
E
P<0.0001
# of MYO10-positive filopodia
150
100
50
0
GFP ctrl
GFP-SPN
F
GFP
F-actin
MERGE
GFP ctrl
GFP-SPN
20 µm
G
P<0.0001
F-actin colocalisation
Pearson's Coefficient
1.0
0.5
0.0
-0.5
-1.0
GFP ctrl
GFP-SPN

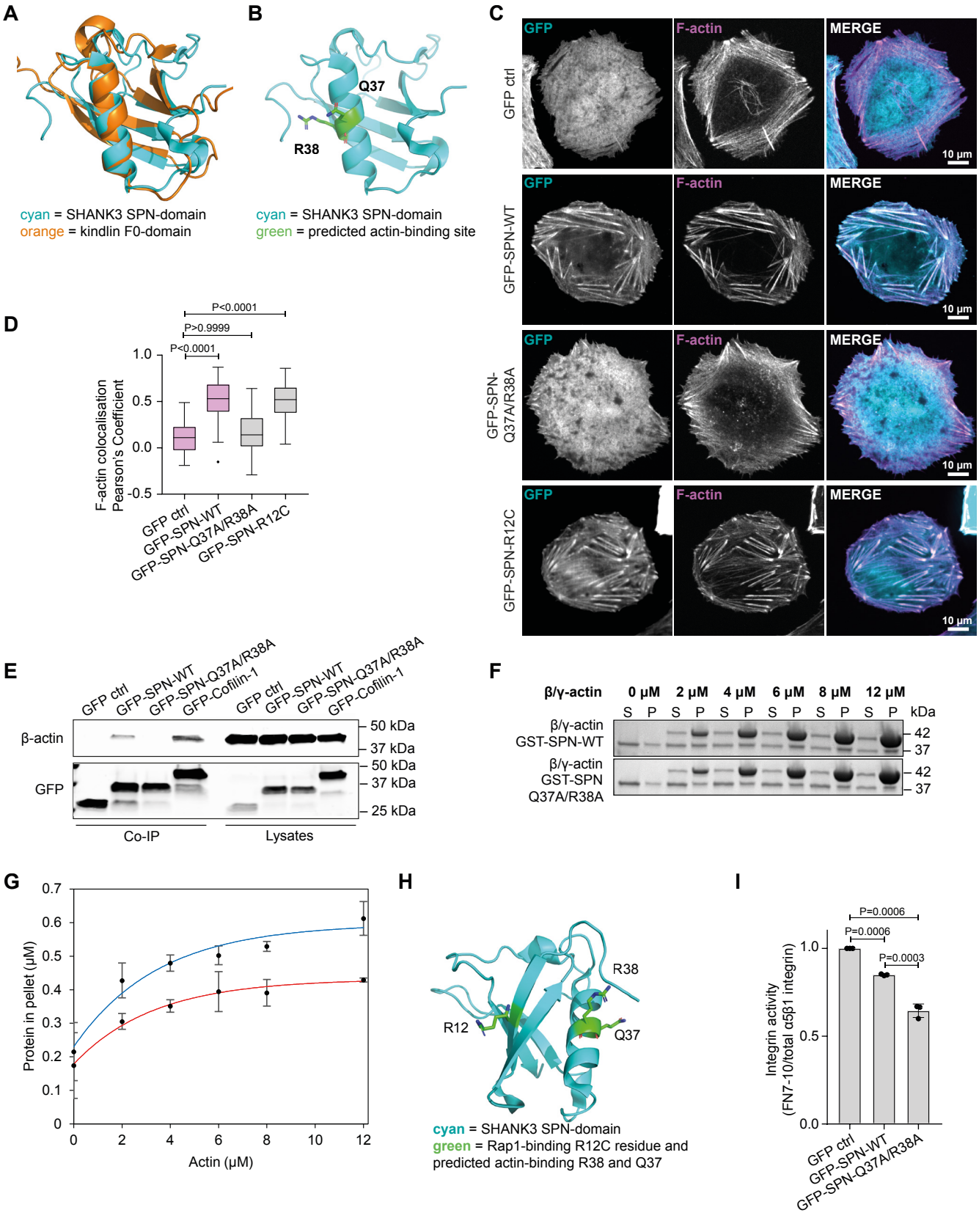
A
cyan = SHANK3 SPN-domain
orange = kindlin F0-domain
B
Q37
R38
cyan = SHANK3 SPN-domain
green = predicted actin-binding site
C
GFP
F-actin
MERGE
GFP ctrl
GFP-SPN-WT
GFP-SPN-Q37A/R38A
GFP-SPN-R12C
10 µm
D
P<0.0001
P>0.9999
P<0.0001
F-actin colocalisation Pearson's Coefficient
1.0
0.5
0.0
-0.5
GFP ctrl
GFP-SPN-WT
GFP-SPN-Q37A/R38A
GFP-SPN-R12C
E
GFP ctrl
GFP-SPN-WT
GFP-SPN-Q37A/R38A
GFP-Cofilin-1
β-actin
GFP
50 kDa
37 kDa
25 kDa
Co-IP
Lysates
F
β/γ-actin
0 µM
2 µM
4 µM
6 µM
8 µM
12 µM
S P
kDa
β/γ-actin GST-SPN-WT
β/γ-actin GST-SPN Q37A/R38A
42
37
G
Protein in pellet (µM)
Actin (µM)
H
R38
R12
Q37
cyan = SHANK3 SPN-domain
green = Rap1-binding R12C residue and predicted actin-binding R38 and Q37
I
P=0.0006
P=0.0006
P=0.0003
Integrin activity (FN7-10/total α5β1 integrin)
1.0
0.5
0.0
GFP ctrl
GFP-SPN-WT
GFP-SPN-Q37A/R38A

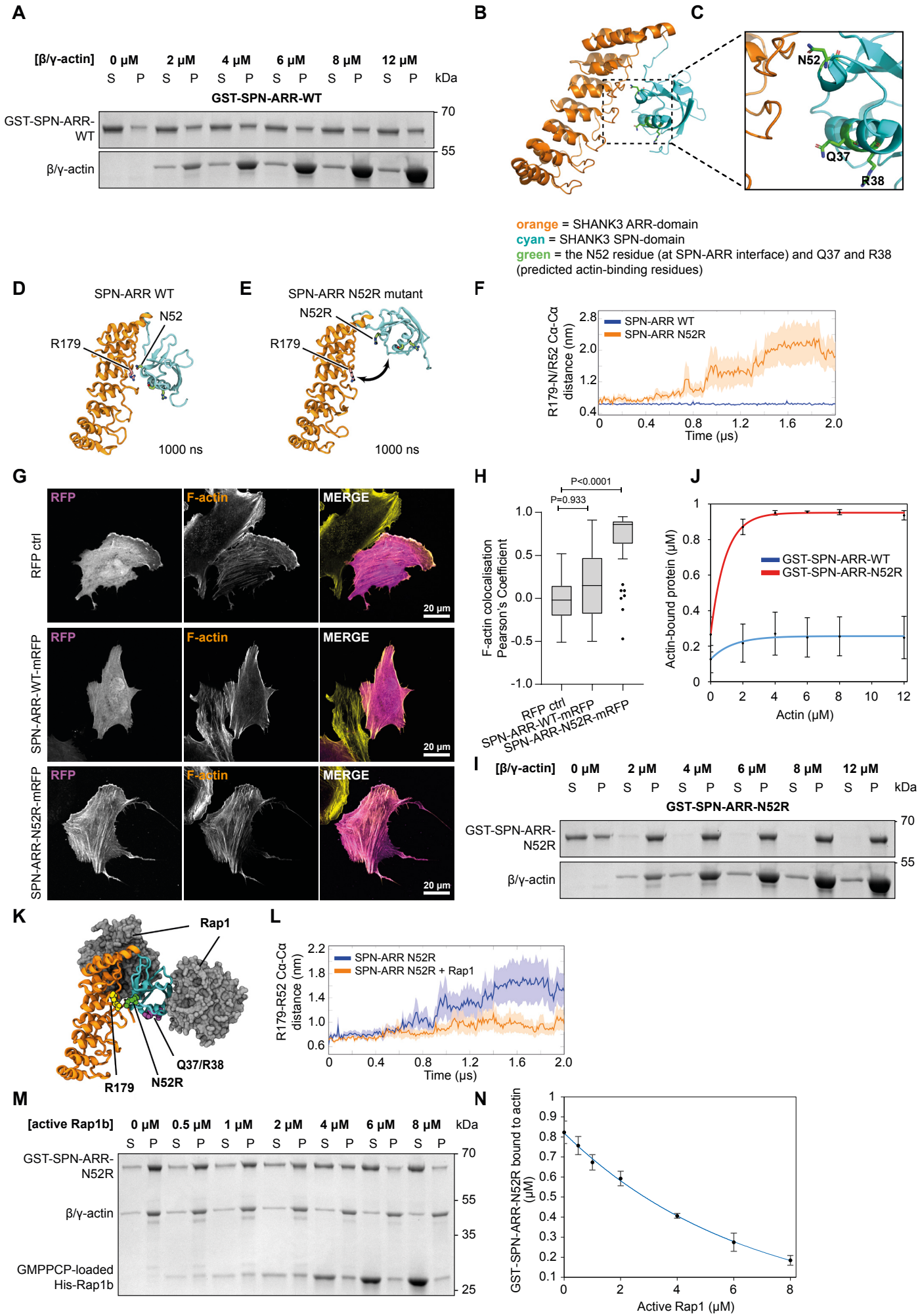
A
[β/γ-actin]
0 μM
2 μM
4 μM
6 μM
8 μM
12 μM
S P S P S P S P S P S P kDa
GST-SPN-ARR-WT
GST-SPN-ARR-WT
β/γ-actin
70
55
B
C
N52
Q37
R38
orange = SHANK3 ARR-domain
cyan = SHANK3 SPN-domain
green = the N52 residue (at SPN-ARR interface) and Q37 and R38 (predicted actin-binding residues)
D
SPN-ARR WT
N52
R179
1000 ns
E
SPN-ARR N52R mutant
N52R
R179
1000 ns
F
R179-N/R52 Cα-Cα distance (nm)
SPN-ARR WT
SPN-ARR N52R
Time (μs)
G
RFP ctrl
SPN-ARR-WT-mRFP
SPN-ARR-N52R-mRFP
RFP
F-actin
MERGE
20 μm
H
P<0.0001
P=0.933
F-actin colocalisation Pearson's Coefficient
RFP ctrl
SPN-ARR-WT-mRFP
SPN-ARR-N52R-mRFP
J
Actin-bound protein (μM)
GST-SPN-ARR-WT
GST-SPN-ARR-N52R
Actin (μM)
I
[β/γ-actin]
0 μM
2 μM
4 μM
6 μM
8 μM
12 μM
S P S P S P S P S P S P kDa
GST-SPN-ARR-N52R
GST-SPN-ARR-N52R
β/γ-actin
70
55
K
Rap1
Q37/R38
R179
N52R
L
R179-R52 Cα-Cα distance (nm)
SPN-ARR N52R
SPN-ARR N52R + Rap1
Time (μs)
M
[active Rap1b]
0 μM
0.5 μM
1 μM
2 μM
4 μM
6 μM
8 μM
kDa
S P S P S P S P S P S P S P S P
GST-SPN-ARR-N52R
β/γ-actin
GMPPCP-loaded His-Rap1b
70
55
35
25
N
GST-SPN-ARR-N52R bound to actin (μM)
Active Rap1 (μM)

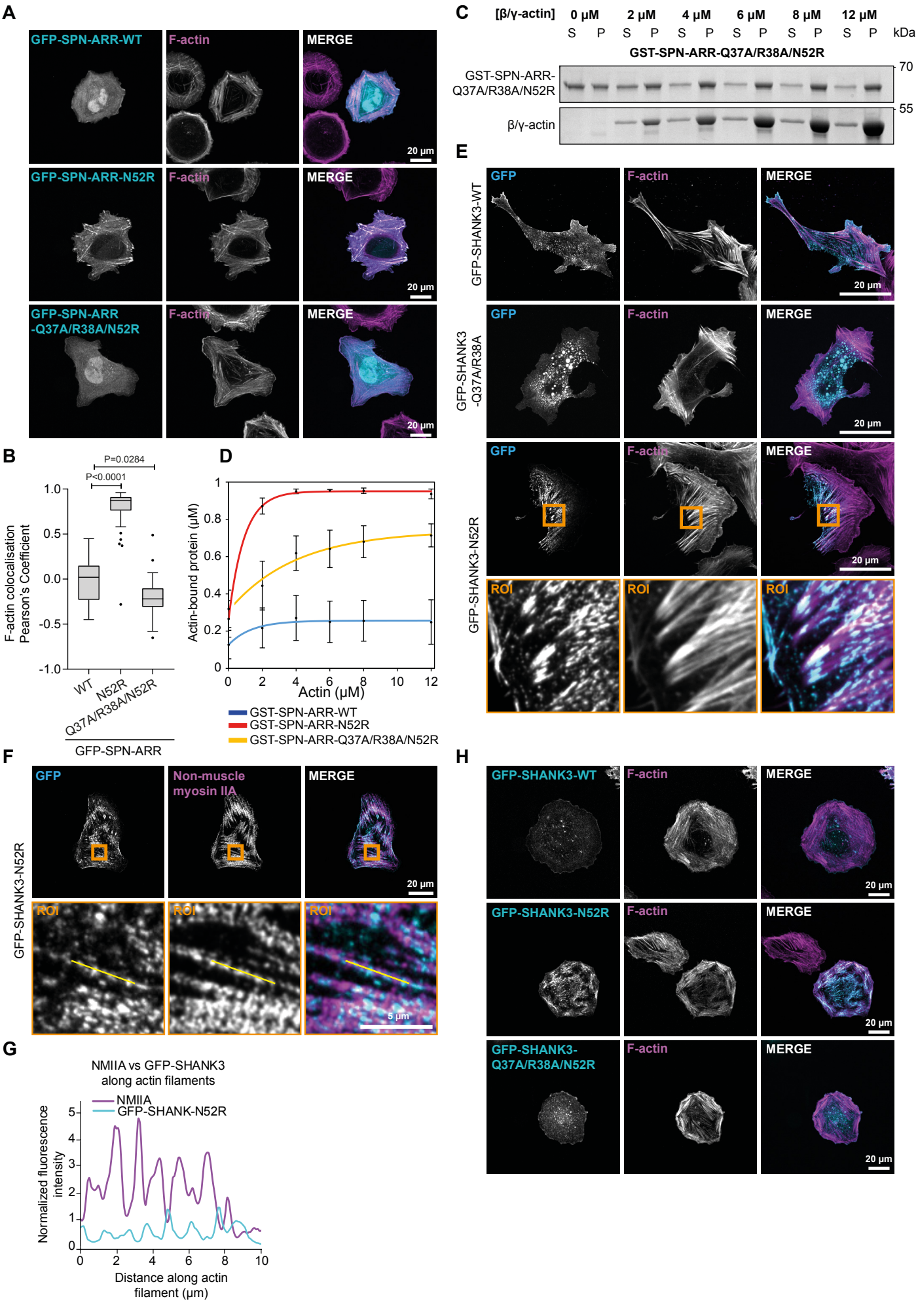
A
GFP-SPN-ARR-WT
F-actin
MERGE
20 μm
GFP-SPN-ARR-N52R
GFP-SPN-ARR
-Q37A/R38A/N52R
B
P=0.0284
P<0.0001
F-actin colocalisation
Pearson's Coefficient
WT
N52R
Q37A/R38A/N52R
GFP-SPN-ARR
C
[β/γ-actin]
0 μM
2 μM
4 μM
6 μM
8 μM
12 μM
S P
kDa
GST-SPN-ARR-Q37A/R38A/N52R
70
55
β/γ-actin
D
Actin-bound protein (μM)
Actin (μM)
GST-SPN-ARR-WT
GST-SPN-ARR-N52R
GST-SPN-ARR-Q37A/R38A/N52R
E
GFP
GFP-SHANK3-WT
GFP-SHANK3
-Q37A/R38A
GFP-SHANK3-N52R
ROI
F
Non-muscle
myosin IIA
5 μm
G
NMIIA vs GFP-SHANK3
along actin filaments
NMIIA
GFP-SHANK-N52R
Normalized fluorescence
intensity
Distance along actin
filament (μm)
H
GFP-SHANK3-WT
GFP-SHANK3-N52R
GFP-SHANK3-
Q37A/R38A/N52R

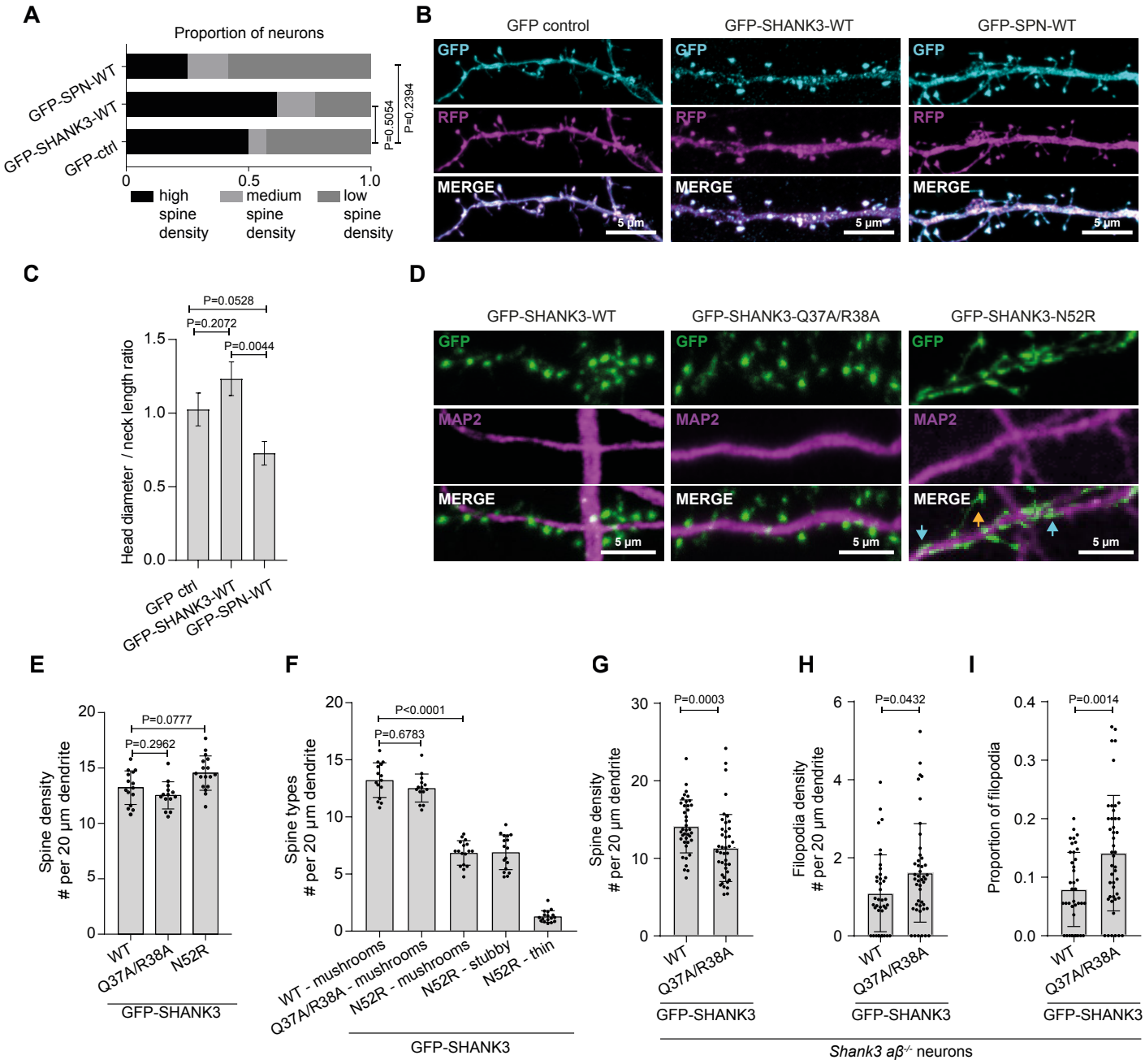
A
Proportion of neurons
GFP-SPN-WT
GFP-SHANK3-WT
GFP-ctrl
P=0.5054
P=0.2394
0
0.5
1.0
high spine density
medium spine density
low spine density
B
GFP control
GFP-SHANK3-WT
GFP-SPN-WT
GFP
RFP
MERGE
5 µm
C
P=0.0528
P=0.2072
P=0.0044
Head diameter / neck length ratio
1.5
1.0
0.5
0.0
GFP ctrl
GFP-SHANK3-WT
GFP-SPN-WT
D
GFP-SHANK3-WT
GFP-SHANK3-Q37A/R38A
GFP-SHANK3-N52R
GFP
MAP2
MERGE
5 µm
E
Spine density
# per 20 µm dendrite
P=0.0777
P=0.2962
20
15
10
5
0
WT
Q37A/R38A
N52R
GFP-SHANK3
F
Spine types
per 20 µm dendrite
P<0.0001
P=0.6783
WT - mushrooms
Q37A/R38A - mushrooms
N52R - mushrooms
N52R - stubby
N52R - thin
GFP-SHANK3
G
Spine density
# per 20 µm dendrite
P=0.0003
30
20
10
0
WT
Q37A/R38A
GFP-SHANK3
H
Filopodia density
# per 20 µm dendrite
P=0.0432
6
4
2
0
WT
Q37A/R38A
GFP-SHANK3
I
Proportion of filopodia
P=0.0014
0.4
0.3
0.2
0.1
0.0
WT
Q37A/R38A
GFP-SHANK3
Shank3 aβ-/- neurons

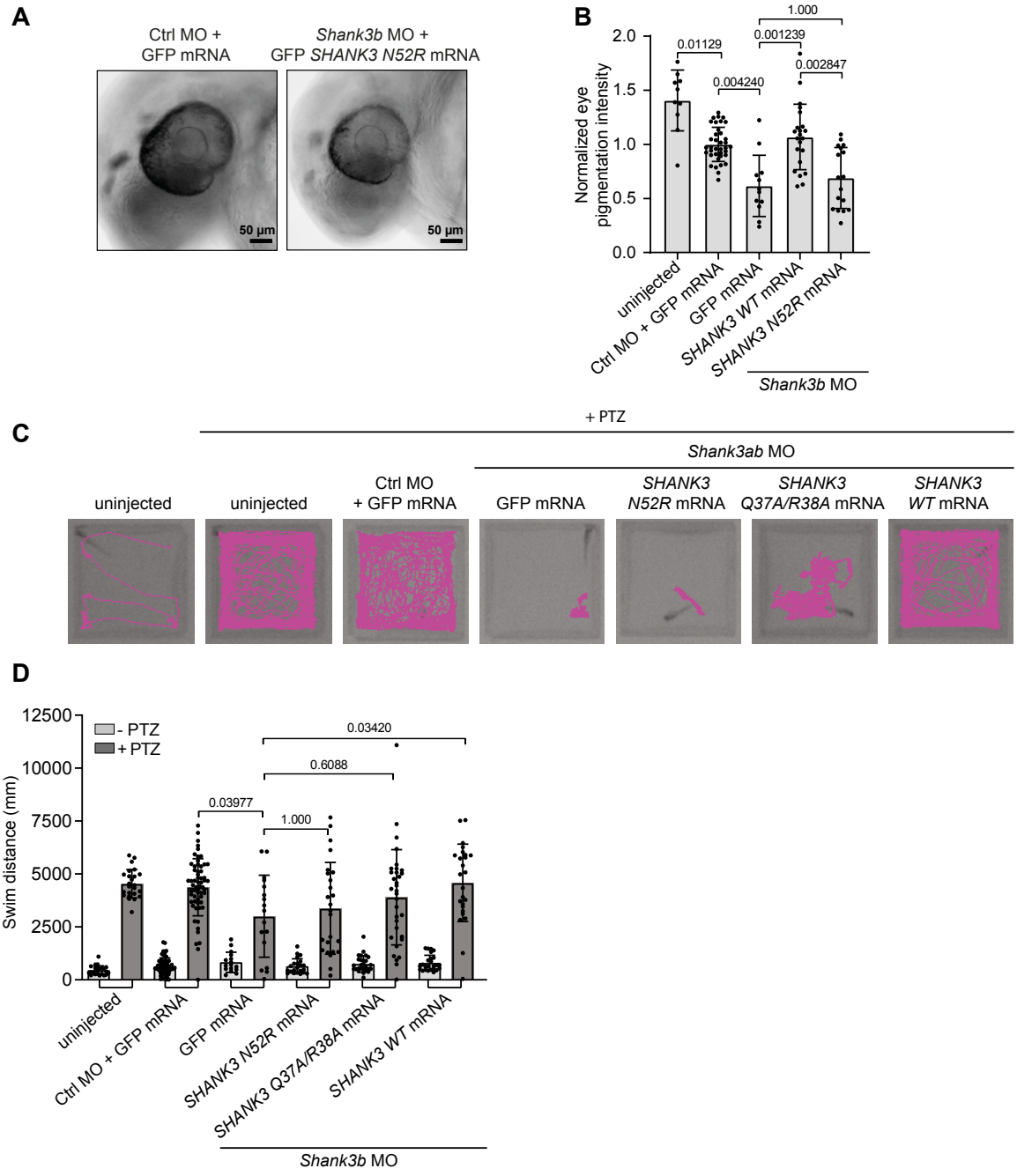
A
Ctrl MO +
GFP mRNA
Shank3b MO +
GFP SHANK3 N52R mRNA
50 µm
50 µm
B
Normalized eye
pigmentation intensity
2.0
1.5
1.0
0.5
0.0
0.01129
0.004240
1.000
0.001239
0.002847
uninjected
Ctrl MO + GFP mRNA
GFP mRNA
SHANK3 WT mRNA
SHANK3 N52R mRNA
Shank3b MO
C
+ PTZ
Shank3ab MO
uninjected
uninjected
Ctrl MO
+ GFP mRNA
GFP mRNA
SHANK3
N52R mRNA
SHANK3
Q37A/R38A mRNA
SHANK3
WT mRNA
D
Swim distance (mm)
12500
10000
7500
5000
2500
0
- PTZ
+ PTZ
0.03420
0.6088
0.03977
1.000
uninjected
Ctrl MO + GFP mRNA
GFP mRNA
SHANK3 N52R mRNA
SHANK3 Q37A/R38A mRNA
SHANK3 WT mRNA
Shank3b MO

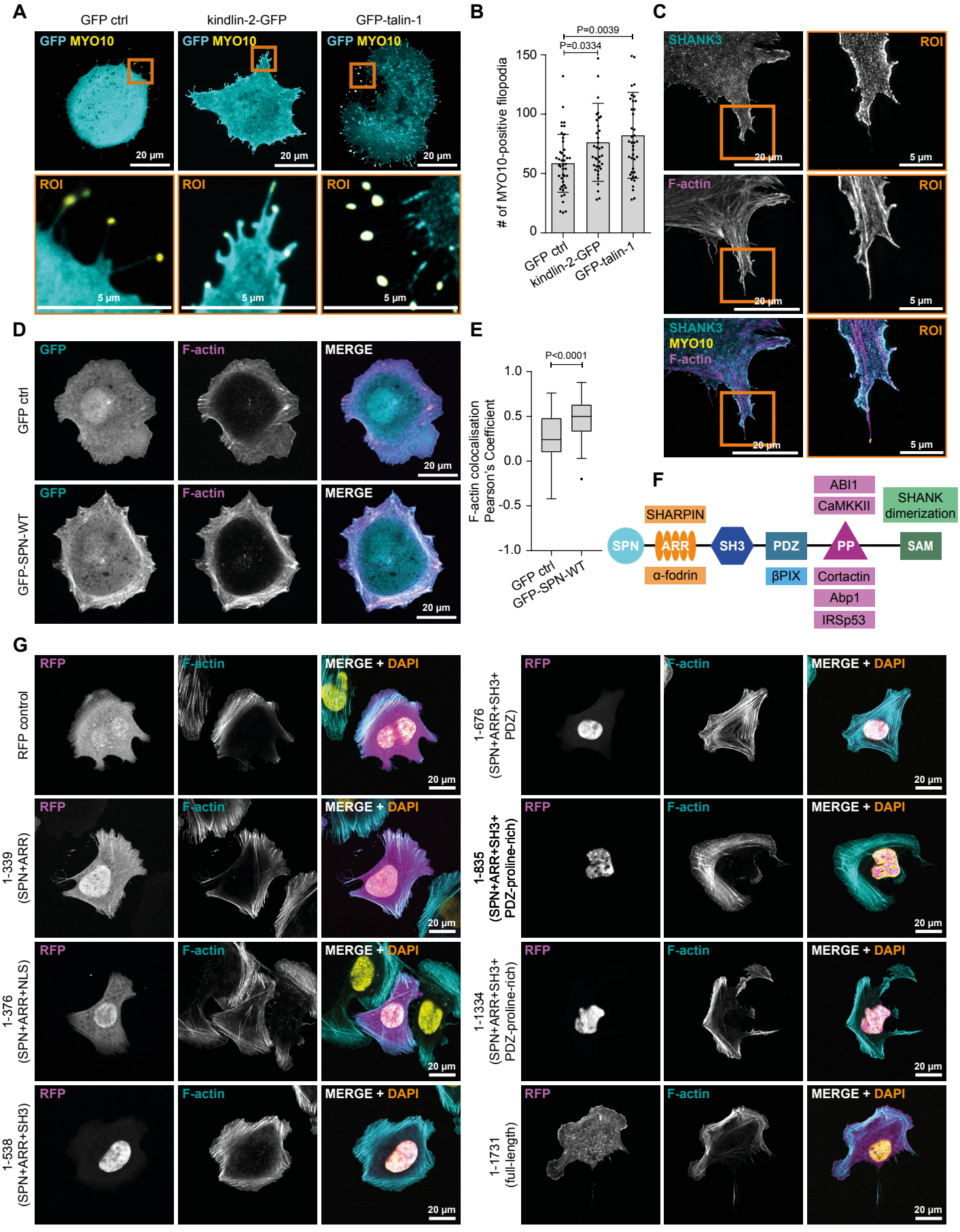
A
GFP ctrl
kindlin-2-GFP
GFP-talin-1
GFP MYO10
ROI
20 µm
5 µm
B
P=0.0039
P=0.0334
# of MYO10-positive filopodia
150
100
50
0
GFP ctrl
kindlin-2-GFP
GFP-talin-1
C
SHANK3
F-actin
ROI
20 µm
5 µm
D
GFP ctrl
GFP-SPN-WT
GFP
F-actin
MERGE
20 µm
E
P<0.0001
F-actin colocalisation
Pearson's Coefficient
1.0
0.5
0.0
-0.5
-1.0
GFP ctrl
GFP-SPN-WT
F
SHARPIN
SPN
ARR
SH3
PDZ
PP
SAM
α-fodrin
βPIX
ABI1
CaMKKII
Cortactin
Abp1
IRSp53
SHANK dimerization
G
RFP control
1-339 (SPN+ARR)
1-376 (SPN+ARR+NLS)
1-538 (SPN+ARR+SH3)
1-676 (SPN+ARR+SH3+ PDZ)
1-835 (SPN+ARR+SH3+ PDZ-proline-rich)
1-1334 (SPN+ARR+SH3+ PDZ-proline-rich)
1-1731 (full-length)
RFP
F-actin
MERGE + DAPI
20 µm

Figure S1. SHANK3 SPN-domain colocalization with actin is inhibited in longer SHANK3 fragments. Related to Figure 1. A, B, Analysis of filopodia formation in U2OS cells co-expressing either GFP control, kindlin-2-GFP or GFP-talin together with MYO10-mCherry and plated on fibronectin for 2 h. Representative bottom plane confocal images (A) and quantification of filopodia number (B) are shown. **C,** Analysis of SHANK3 localization along filopodia in U2OS cells co-expressing GFP-SHANK3-WT and MYO10-mCherry plated on fibronectin for 2 h and stained for F-actin (SiR-actin). **D, E,** Analysis of F-actin (attophalloidin-647) and GFP colocalization in HEK293 cells expressing either GFP control or GFP-SPN and plated on fibronectin for 1 h. Representative bottom plane confocal images (D) and quantification (E) using the coloc2 ImageJ plugin from one experiment are shown. **F,** Schematic of SHANK3 functional domains and each domain's actin-related binding partners. **G,** Analysis of SHANK3 subcellular localization in U2OS cells expressing different SHANK3-mRFP fragments, plated on fibronectin (3-4 h) and stained for F-actin (attophalloidin-647). Representative bottom plane confocal images from two independent experiments are shown. All representative micrographs and data are from n = three independent experiments unless otherwise indicated. Data are mean ± s.d. (B) or presented as Tukey box plots (E). Statistical analyses: (B) Kruskal-Wallis non-parametric test and Dunn's multiple comparisons post hoc test. (E) Mann-Whitney two-tailed T-test. Number of cells analyzed: (B) 43 cells (GFP ctrl), 38 (kindlin-2-GFP) and 41 (GFP-talin). (E) 79 (GFP ctrl) and 84 (GFP-SPN).

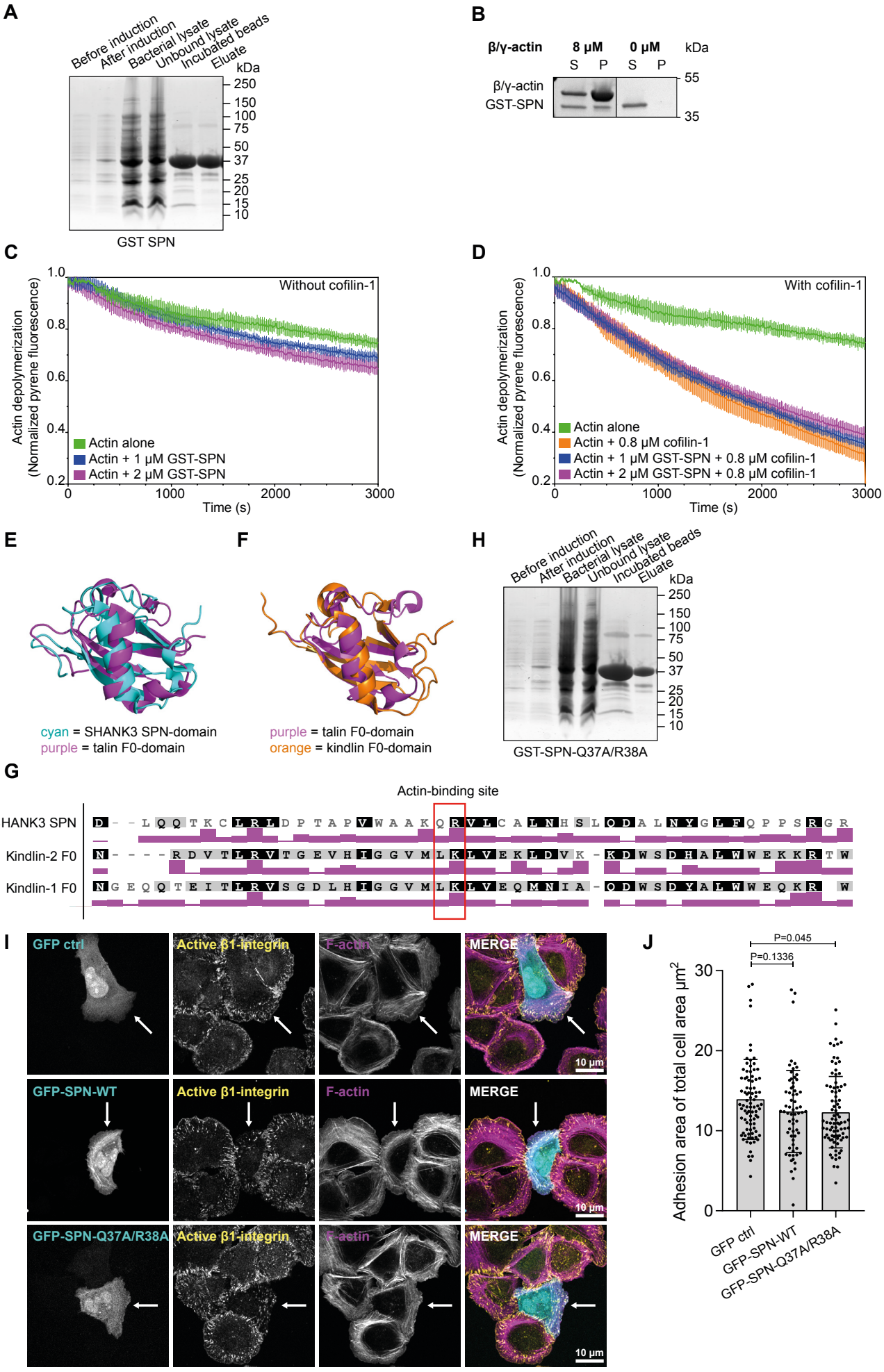
A
Before induction
After induction
Bacterial lysate
Unbound lysate
Incubated beads
Eluate
kDa
250
150
100
75
50
37
25
20
15
10
GST SPN
B
β/γ-actin
8 μM
0 μM
kDa
S P S P
β/γ-actin
GST-SPN
55
35
C
Without cofilin-1
Actin depolymerization (Normalized pyrene fluorescence)
Actin alone
Actin + 1 μM GST-SPN
Actin + 2 μM GST-SPN
Time (s)
D
With cofilin-1
Actin alone
Actin + 0.8 μM cofilin-1
Actin + 1 μM GST-SPN + 0.8 μM cofilin-1
Actin + 2 μM GST-SPN + 0.8 μM cofilin-1
Time (s)
E
cyan = SHANK3 SPN-domain
purple = talin F0-domain
F
purple = talin F0-domain
orange = kindlin F0-domain
H
Before induction
After induction
Bacterial lysate
Unbound lysate
Incubated beads
Eluate
kDa
GST-SPN-Q37A/R38A
G
Actin-binding site
SHANK3 SPN
Kindlin-2 F0
Kindlin-1 F0
I
GFP ctrl
Active β1-integrin
F-actin
MERGE
GFP-SPN-WT
GFP-SPN-Q37A/R38A
10 μm
J
P=0.045
P=0.1336
Adhesion area of total cell area μm²
GFP ctrl
GFP-SPN-WT
GFP-SPN-Q37A/R38A

Figure S2. SHANK3 SPN does not affect actin filament stability. Related to Figure 2. A, Recombinant GST-tagged SPN protein was expressed and purified from E. coli. Samples were resolved by SDS-PAGE and visualized by Coomassie Blue staining. Figure shows a representative gel. **B,** Analysis of GST-SPN (1 μM) interaction with β/γ-actin filaments (8 μM) in co-sedimentation assays at low speed centrifugation (19.000 rpm for 30 min). S, supernatant fraction; P, pellet fraction; n = 1 experiment. **C, D,** Spontaneous (C) and cofilin-induced (D) disassembly of β/γ-actin (4 μM of pre-polymerized β/γ-pyrene-actin) filaments in the presence of GST-SPN (1 or 2 μM) after a 5-minute incubation. Actin filament disassembly was initialized by addition of 6 μM vitamin D binding protein (C, D) and induced with 0.8 μM cofilin-1 (D). Actin depolymerization was monitored by a decrease in pyrene-actin fluorescence. **E, F,** Superimposition of the talin F0-domain (PDB: 2KC1) with either SHANK3 SPN (PDB: 5G4X) (F) or the kindlin F0-domain (PDB: 2KMC). **G,** Sequence alignment between the SHANK3 SPN and the kindlin-1/2 F0-domains. The heights of the purple colored bars represent amino acid pI (isoelectric point) values. The values are normalized such that the amino acid with the lowest PI has a value 0 and the highest a value of 1. Other amino acid's values are interpolated to linearly fit this range and shown to highlight similarities in the local charge distribution of the actin binding site residues. **H,** Recombinant GST-SPN-Q37A/R38A protein were expressed and purified from E. coli. Samples were resolved by SDS-PAGE and visualized by Coomassie Blue staining. Figure shows a representative gel. **I, J,** Analysis of integrin activity in U2OS cells co-expressing either GFP control, GFP-SPN-WT or GFP-SPN-Q37A/R38A plated on fibronectin for 1,5 h. Representative bottom plane confocal images (I) and quantification of area positive for active integrin β1 staining of total cell area (J) are shown. White arrows highlight cells expressing GFP-tagged constructs. All data are from three independent experiments unless otherwise indicated. Error bars represent s.d. Statistical analyses: (J) Kruskal-Wallis non-parametric test and Dunn's multiple comparisons post hoc test. Number of cells analyzed: (J) 88 (GFP ctrl), 66 (GFP-SPN-WT) and 88 (Q37A/R38A).

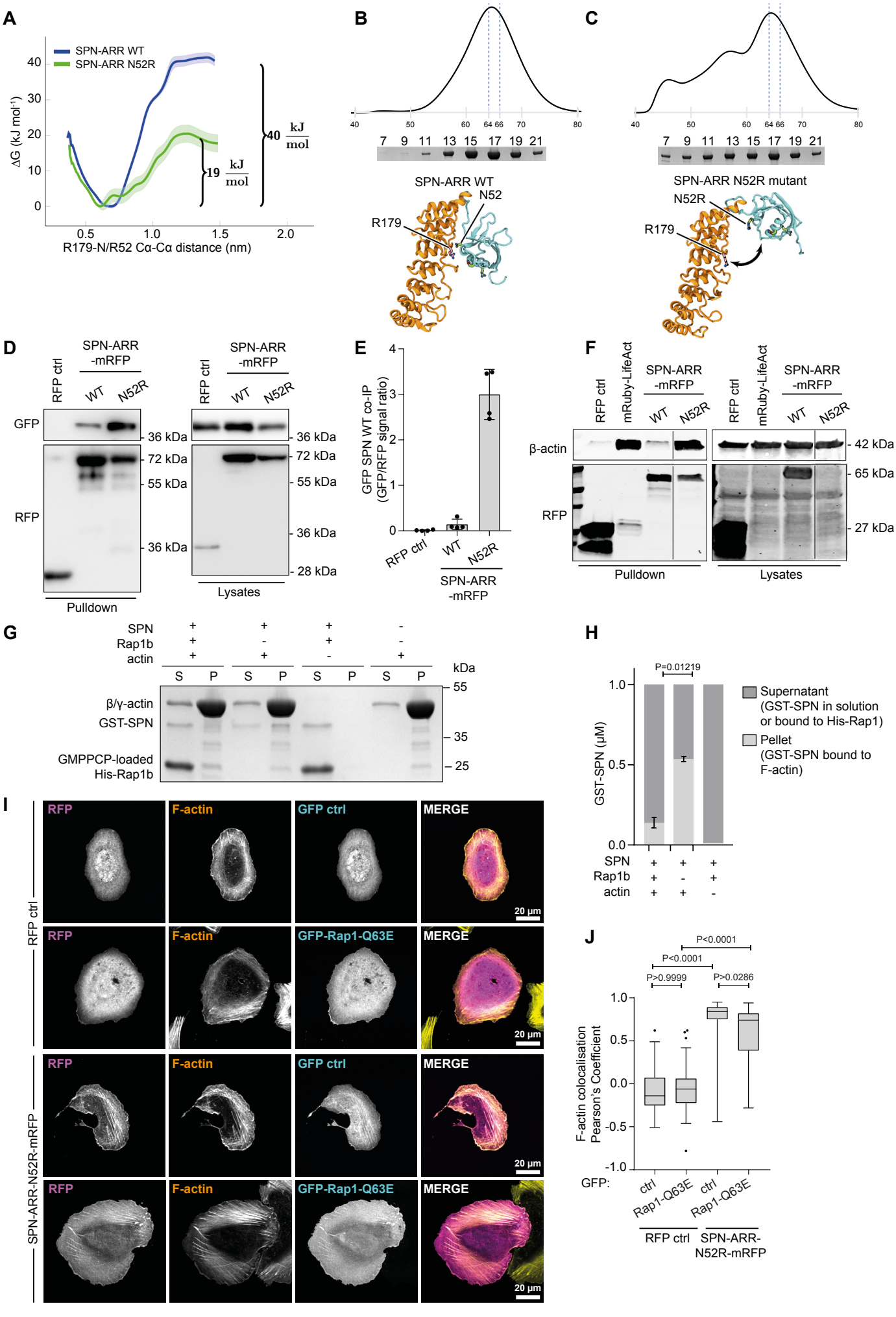
A
SPN-ARR WT
SPN-ARR N52R
ΔG (kJ mol-1)
40
30
20
10
0
19 kJ/mol
40 kJ/mol
0.5
1.0
1.5
2.0
R179-N/R52 Cα-Cα distance (nm)
B
40
50
60
64 66
70
80
7 9 11 13 15 17 19 21
SPN-ARR WT
N52
R179
C
40
50
60
64 66
70
80
7 9 11 13 15 17 19 21
SPN-ARR N52R mutant
N52R
R179
D
RFP ctrl
SPN-ARR -mRFP
WT
N52R
GFP
RFP
36 kDa
72 kDa
55 kDa
36 kDa
36 kDa
72 kDa
55 kDa
36 kDa
28 kDa
Pulldown
Lysates
E
GFP SPN WT co-IP (GFP/RFP signal ratio)
4
3
2
1
0
RFP ctrl
WT
N52R
SPN-ARR -mRFP
F
RFP ctrl
mRuby-LifeAct
SPN-ARR -mRFP
WT
N52R
β-actin
RFP
42 kDa
65 kDa
27 kDa
Pulldown
Lysates
G
SPN
Rap1b
actin
S P S P S P S P
kDa
β/γ-actin
GST-SPN
GMPPCP-loaded His-Rap1b
55
35
25
H
P=0.01219
GST-SPN (μM)
1.0
0.5
0.0
Supernatant (GST-SPN in solution or bound to His-Rap1)
Pellet (GST-SPN bound to F-actin)
SPN
Rap1b
actin
I
RFP ctrl
SPN-ARR-N52R-mRFP
RFP
F-actin
GFP ctrl
GFP-Rap1-Q63E
MERGE
20 μm
J
P<0.0001
P<0.0001
P>0.9999
P>0.0286
F-actin colocalisation Pearson's Coefficient
1.0
0.5
0.0
-0.5
-1.0
GFP:
ctrl
Rap1-Q63E
ctrl
Rap1-Q63E
RFP ctrl
SPN-ARR-N52R-mRFP

Figure S3. Active Rap1 inhibits SHANK3-actin interaction. Related to Figure 3. A, Free energy profiles of the opening of SHANK3 SPN-ARR. The data are calculated through Umbrella Sampling atomistic MD simulations (Systems S5 and S6 in Table, see methods). The two SHANK3 domains are bound at the distance of 0.6 nm, and in the open conformation at 1.4 nm. **B, C,** Gel filtration elution profile of GST-SPN-ARR proteins. GST-SPN-ARR-WT (B) elutes as a single peak around fraction 17 (64-66 ml of the elution), most probably representing a dimeric protein in a closed conformation. GST-SPN-ARR-N52R (C) elutes with a major peak at fraction 17, but the protein is also present in earlier fractions probably representing the protein populations with more open conformations. **D, E,** Representative RFP-trap pulldown in HEK293 cells co-expressing GFP-SPN-WT together with either RFP control (negative control), SPN-ARR-WT-mRFP or SPN-ARR-N52R-mRFP (D) and quantification (E). Input lysates and IP samples were analyzed using RFP and GFP antibodies as indicated. Data are representative of four independent experiments. **F,** RFP-trap pulldown in HEK293 cells expressing either RFP control (negative control), mRuby-LifeAct (positive control), SPN-ARR-WT-mRFP or SPN-ARR-N52R-mRFP. Input lysates and IP samples were analyzed using β-actin and RFP antibodies as indicated. **G, H,** Analysis of GST-SPN (1 μM) interaction with β/γ-actin filaments (12 μM) in the presence or absence of active GMPPCP-loaded (GTP-analogue) His-Rap1b (4 μM). A representative high-speed co-sedimentation experiment (G) and quantification of the proportion of SPN in the pellet fraction (P, represents SPN bound to actin) versus the supernatant fraction (S, represents soluble protein not bound to actin) (H) are shown. The addition of active His-Rap1b increases the amount of GST-SPN remaining in the supernatant and not co-sedimenting with actin. Five independent experiments. **I, J,** Analysis of F-actin (SiR-actin) and RFP colocalization in U2OS cells co-expressing RFP control or SPN-ARR-N52R-mRFP together with either GFP control or GFP-Rap1-Q63E. Cells were plated on fibronectin-coated glass-bottom dishes (3-4 h). Representative bottom plane confocal images (I) and quantification (J) using the coloc2 ImageJ plugin are shown. All data are from three independent experiments unless otherwise indicated. Data are mean ± s.d. (E), ± s.e.m. (H) or displayed as Tukey box plots (J). Number of cells: (J) 63 (RFP ctrl+GFP ctrl), 65 (RFP ctrl+GFP-Rap1-Q63E), 68 (SPN-ARR-N52R-mRFP+GFP ctrl) and 64 (SPN-ARR-N52R-mRFP+GFP-Rap1-Q63E). Statistical analysis: (J) Kruskal-Wallis non-parametric test and Dunn's multiple comparisons post hoc test.

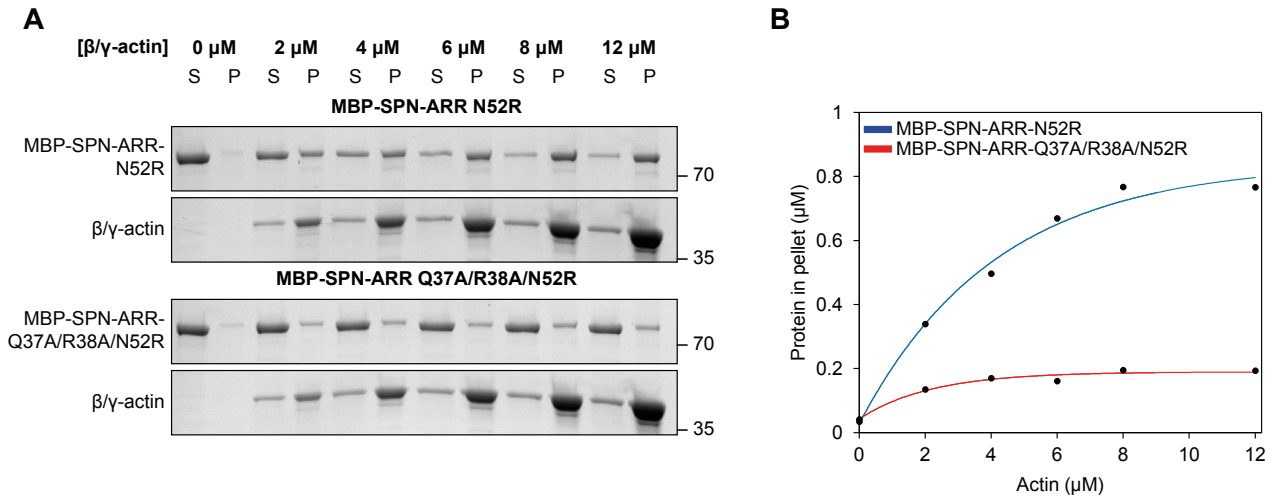

Figure S4. The Q37A/R38A mutation interferes with actin binding even in the presence of the fold opening N52R mutation. Related to Figure 4. A, B, Analysis of MBP-tagged SPN-ARR-N52R (1 µM) and SPN-ARR-Q37A/R38A/N52R (1 µM) binding to β/γ-actin filaments (0, 2, 4, 6, 8 and 12 µM) in a high-speed co-sedimentation assay. Representative example of protein binding (A) and quantification (B). S, supernatant fraction; P, pellet fraction.

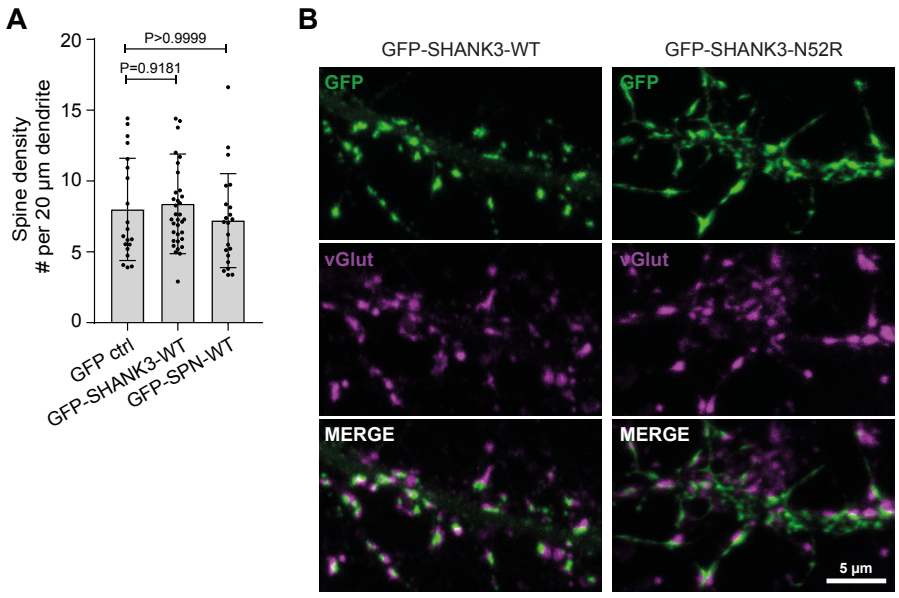

Figure S5. The effects of GFP-SHANK3 mutants and GFP-SPN in WT primary neurons. Related to Figure 5. A, Quantifications of spine density of WT primary rat hippocampal neurons expressing the indicated constructs and fixed at DIV16-18. Representative maximum intensity projection confocal images shown in Figure 6B. **B,** Representative maximum intensity projection confocal images of WT primary rat hippocampal neurons expressing the indicated constructs and fixed at DIV16-18. The neurons were stained with the vesicular glutamate transporter (vGlut). Data represent mean ± s.d : spine density in secondary dendrites; (A) n = 20 (GFP ctrl), 35 (GFP-SHANK3-WT) and 22 (GFP-SPN-WT) neurons. Statistical analysis: (A) Kruskal-Wallis non-parametric test and Dunn's multiple comparisons post hoc test.